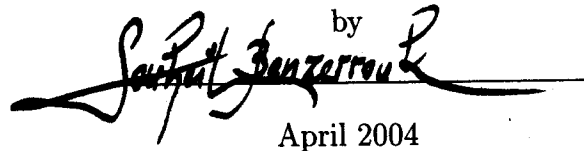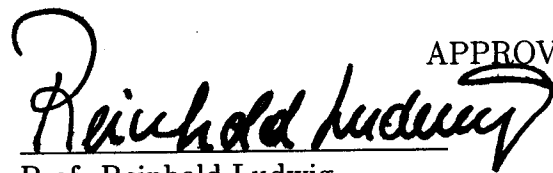# Feasibility Study of Infrared Detection of Defects in Green-State and Sintered PM Compacts

by

Souheil Benzerrouk

A Thesis

Submitted to the Faculty

of the

WORCESTER POLYTECHNIC INSTITUTE

in partial fulfillment of the requirements for the

Degree of Master of Science

in

Electrical and Computer Engineering

by

Souheil Benzerrouk

April 2004

APPROVED:

Prof. Reinhold Ludwig
ECE Department,
Thesis Advisor.
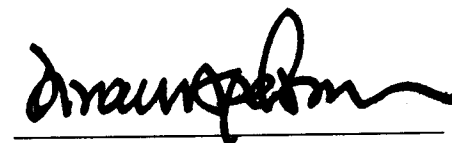
Prof. Diran Apelian
ME Department,
Committee Member.

Prof. John Sullivan, Jr
ECE Department,
Committee Member.

Prof. Fred Looft
ECE Department,
Department Head.

Abstract

The electric Joule heating of solid materials through direct current excitation can be used to generate a temperature profile throughout a powdermetallic (P/M) compact. When recording the surface temperature distribution with an infrared (IR) camera important information regarding the integrity of the sample can be gained.

This research will concentrate on the formulation of a mathematical model capable of predicting the temperature distribution and heat flow behavior in P/M parts and its relations to the supplied current, injection method, geometric shape as well as the thermo-physical properties. This theoretical model will subsequently be employed as a tool to aid in the actual measurements of infrared signatures over the sample surface and their correlation with the detection of surface and subsurface flaws.

In this work we will develop the theoretical background of IR testing of green-state and sintered P/M compacts in terms of stating the governing equations and boundary conditions, followed by devising analytical and numerical solutions. Our main emphasis is placed on modeling various flaw sizes and orientations in an effort to determine flaw resolution limits as a function of minimally detectable temperature distributions.

Preliminary measurements with controlled and industrial samples have shown that this IR testing methodology can successfully be employed to test both green-state and sintered P/M compacts.

Acknowledgement

I cannot express the gratitude I have to my thesis advisor, Prof. Reinhold Ludwig. Without his guidance, patience and encouragements I would not have been able to complete this work. It has been a privilege to work with Prof. Ludwig. His dedication, enthusiasm and talent have certainly made a lasting impression on me.

I would like to express my gratitude to Prof. Diran Apelian for providing valuable insights during the course of this project and for sharing his visions for the future of this work. I would also like to thank Prof. John Sullivan Jr. for consenting to be part of my thesis committee and for providing valuable suggestions.

I thank Richard Scott (Nichols Portland) and Hannes Traxler (PLANSEE Aktiengesellschaft) for providing the needed PM samples to complete this research.

I am grateful to my friends and colleagues in the RF laboratory Sonam Tobgay, Tim Fisher, Rostislav Lemdiasov and Pavlo Fedorenko for making the environment in the lab pleasant and friendly. Specially I would like to thank my good friend and co-worker Aghogho Obi for his untiring help with LaTeX making this thesis possible in this format. I also thank Georg Leuenberger who has done the previous research on this project and who helped me with the background material.

Finally I extend my outmost gratitude to my friends and colleagues at Energetiq Technology Inc., Dr. Don Smith, Dr. Stephen Horne, Matt Besen, Ron Collins and Paul Blackborow for their words of encouragement and untiring help throughout my graduate career.

Dedications

This humble work is dedicated to:

My wonderful parents who taught me the importance of seeking knowledge and seeking the truth. My father Mohamed Benzerrouk who is my model in many aspects of life and my mother Hassiba whose goodness and character are beyond any words.

My sisters Abla and Ismahane who supported me throughout life with unlimited kindness, warmth and thoughtfulness.

My brothers M'hamed and Youcef who show me the outmost respect even with the distance that separates us.

My extended family whose bond gave me the strength and desire to succeed.

The friends I am blessed with, Djamel Hamiroune and his family, Amine Laredj and his family, Omar Yahiaoui and Toufik Bourkiche and others with whom I shared memorable times.

Last, Algeria who has lived under a criminal occupation then a ruthless junta, my prayers for better days and a return to the due place. I also pray for my people in Palestine and other places whose blood is being shed everyday. May Allah s.w.t. deliver them from tyranny.

Souheil Benzerrouk

Contents

List of Figures

List of Tables

Chapter 1

Introduction

1.1 Background

Powder metallurgy (P/M) is a manufacturing approach, where high quality metal parts are made by compressing mixtures of metal powders and lubricants under high pressure. The subsequent sintering process yields components with sufficient strength and geometric precision that compete with parts made with less cost effective techniques such as machining, casting or forging.

Among the benefits of the P/M process we find versatility, efficiency and greater control over the material constituents. These attributes are making this approach the technology of choice in the automotive industry where manufacturers are constantly improving performance while concomitantly lowering costs. Furthermore, the introduction of new structural and physical properties are possible, enable the P/M industry to extend the applications beyond the automotive sector to more diverse markets such as aerospace, medicine and nuclear power generation.

Figure 1.1 depicts a standard P/M manufacturing line. The process is appealing to industry in the sense that near net-shape parts rarely require off-line operations.

Hence, the manufacturing of parts becomes more cost effective and environmentally friendly.

The P/M manufacturing process requires three basic steps and several secondary operations. The three key operations include

- Powder mixing (combining metal powder with lubricants)

- Forming (compacting in a press)

- Sintering (heat treatment of the compacts)
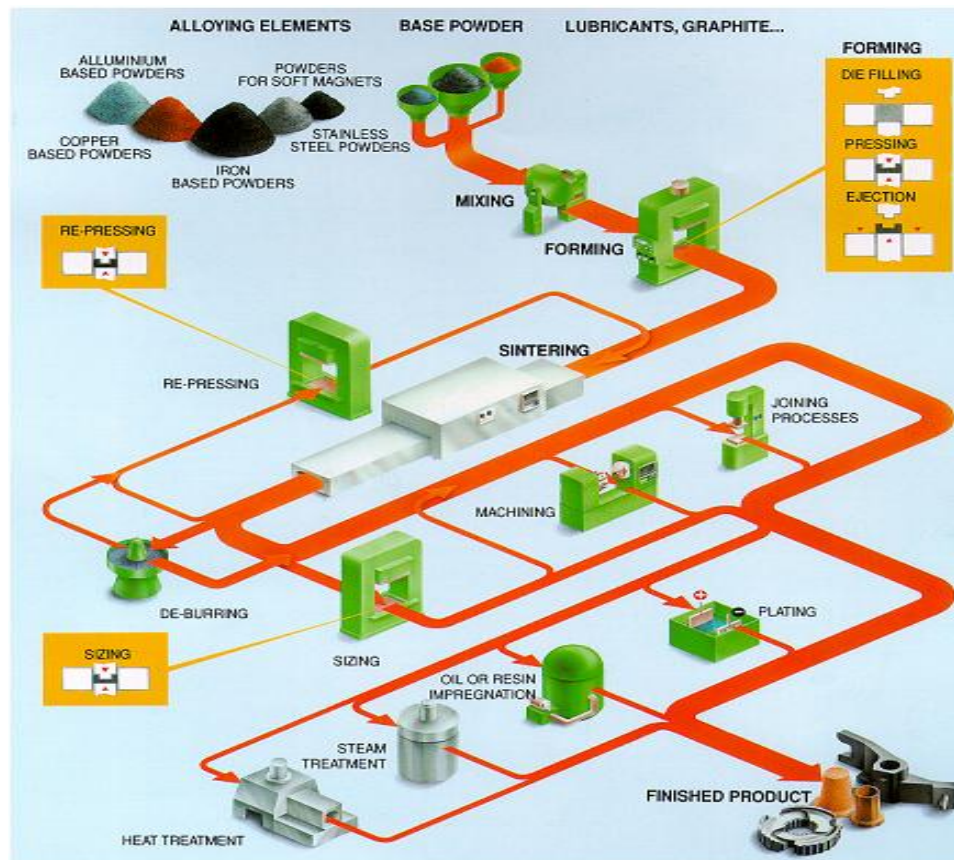
Figure 1.1: Generic manufacturing steps in the production of P/M samples (courtesy of GKN Sinter Metals).

Part constituents or powders are mixed in a blender as shown in Figure 1.2 to produce alloys with specific physical properties. In addition to the basic powder ingredients,

lubricants are added in this step. The purpose of lubricants is to reduce friction between the powder particles and also between the compact and the die wall in the press. This is done in an effort to maximize the energy transfer and maintain the integrity of the part after press ejection.
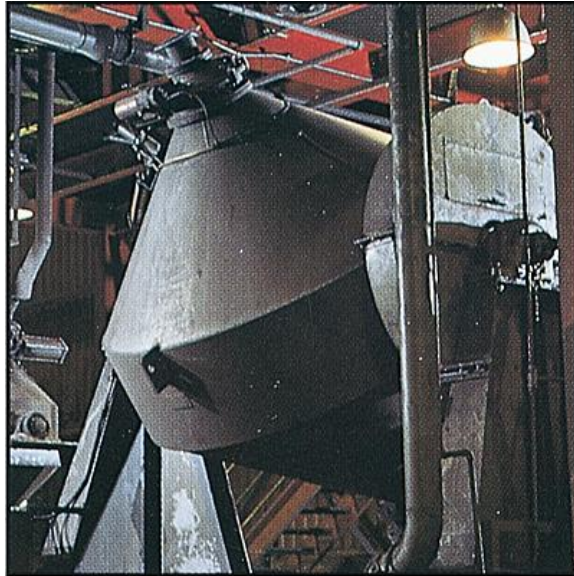
Figure 1.2: Mixing operation: double cone blender (Courtesy of GKN Sinter Metals).

After mixing, the part will be formed through a compaction process. A press is employed to shape the part and compact it to a prescribed pressure to achieve a specific density. Typically a three-piece set constitutes a press: an upper punch to pressurize, a lower punch to position and control the amount of powder in the die, and a die to shape the part.

Compaction can be accomplished by using either a single punch or double punch action, and in one of two modes warm or standard compaction [26]. Figure 1.3 illustrates the forming operation in a single-level part with double punch. An external feed shoe is employed to introduced powder into the die. This operation will be aided by the lower punch to insure that the powder is uniformly distributed in the die. Thereafter, the feed shoe is removed and very high pressure is applied through the

motion of both punches towards the center of the die. After the desired pressure is reached, the part is formed and the upper punch is removed while the lower one moves upwards pushing the green-state sample out of the die and away from the press by means of a feed shoe.
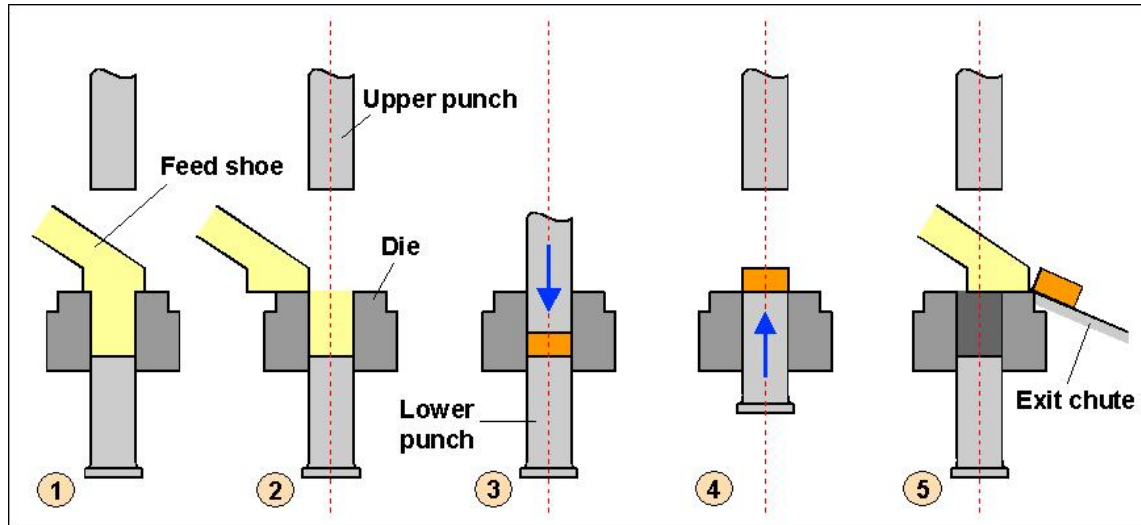
Figure 1.3: Compaction steps in a double punch press (Courtesy of GKN Sinter Metals).

The green-state sample at this stage is extremely fragile as there is no bonding agent between the powder particles other than the weak bonds created by the compaction. The manufacturing of complex, multilevel parts such as gears requires a high degree of sophistication and control during this step. Here punches are made of multiple moving parts to allow powder transfer between levels, this process helps accomplish uniform densities and prevents cracks, especially in corners. The problem of cracking in P/M is the major quality problem the industry faces and great effort is exerted to thoroughly investigate its causes and devise prevention methods.

Figure 1.4 depicts a complex multilevel part that require double punch pressing and simple parts that can easily be produced using single punch press.

Figure 1.4: Various P/M parts: complex multi-level gear and uniform density cylinders.

The green-state part is then transferred to the sintering process where it is heated in a furnace to temperatures slightly below the melting point of the material. This will result in the formation of bonds between the powder particles and consequently will result in the strengthening of the parts, greatly improving their mechanical properties.

Sintering is a three-step process as illustrated in Figure 1.5. First, lubricant and other additives are removed through evaporation: it is accomplished by pre-heating the parts slowly. Thereafter, the compacts are heat treated for several hours to the highest possible temperature to form inter-particle bonds. This step is considered the main stage in sintering. The temperature is then slowly reduced in a controlled manner to prevent thermal shock, which may result in distortions or cracking: it is called the cooling stage.
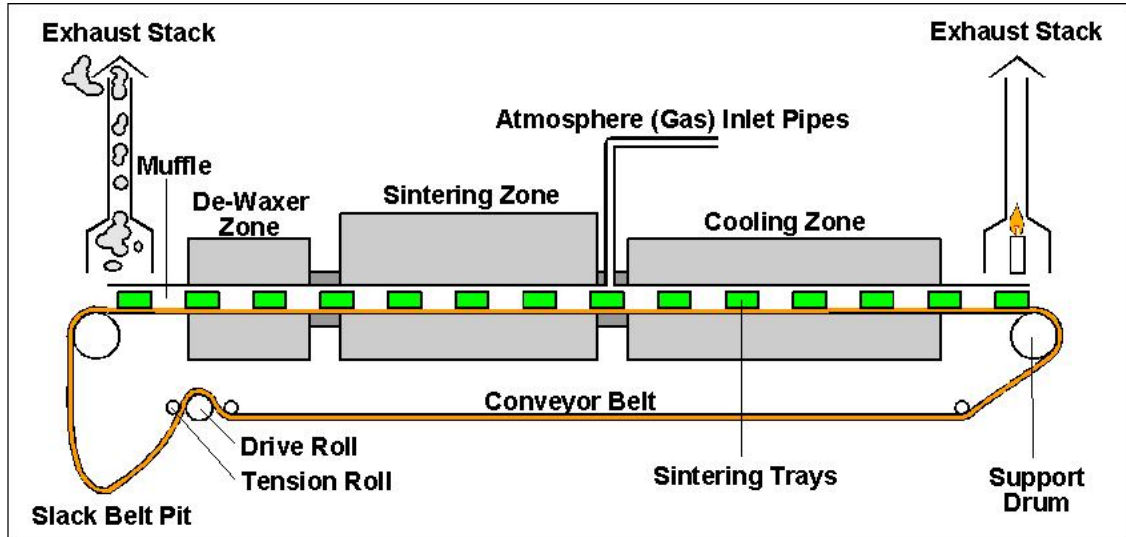
Figure 1.5: Generic sintering furnace (Courtesy of GKN Sinter Metals).

At the end of the sintering step a finished part is produce with mechanical properties similar to a part manufactured with other metal working techniques. Several secondary operations might be required to meet a specific set of requirements such as hardness or corrosion resistance. These operations include sizing, machining, tumbling, oil impregnation, steam treatment, and heat treatment.

1.2 Quality Control during the P/M Manufacturing Process

Recent years have seen a rapid growth in the manufacturing of high volume, complex P/M compacts for a wide range of applications. Increasingly, the manufacturing process of compaction in sophisticated mechanical presses followed by sintering is becoming difficult to control in a manner that assures high-quality finished products at competitive cost points. Therefore, quality assurance is becoming an integral part of this process.

Complex P/M production demands quality assurance throughout the entire manufacturing cycle of the compacts. Ideally, the quality assessment should be conducted in a short period of time with high reliability and at lowest possible cost. Since it is desirable to administer these tests as early as possible in the manufacturing cycle, non-destructive evaluation (NDE) has gained an increasingly important role. Unfortunately, a careful review of most currently employed NDE techniques has shown that most of these techniques cannot directly be applied to the P/M industry without major modifications. For instance, it was found that a generally applicable NDE methodology for both pre- and post-sintered compact inspection simply does not exist at reasonable cost.

1.2.1   NDE Evaluation Methods

As a special metal working technique P/M shares basic quality requirements with other techniques such as casting or forging. These requirements include dimensions, weight, strength, structural integrity and purity. In addition to the basic requirements, P/M compacts require the verification of their density. This is not limited to average density only, but, perhaps more importantly, to the density distribution throughout the compact [1].

The following paragraphs will introduce the most widely used NDE methods to enable us to conduct a comparative study and identify the pros and cons of each methodology.

Eddy Current

In standard eddy current testing, a circular coil excited by an alternating current (AC) source is placed in close proximity to an electrically conductive, non-ferromagnetic specimen as illustrated in Figure 1.6. The AC current in the coil generates a time-varying magnetic field, which interacts with the sample and induces circulating cur-

rents called eddy currents in accordance with the well-known Maxwell-Faraday law
[19]. The eddy currents induced in the material create a magnetic field which op-
poses the primary field (Lenz's law) causing a reduction in the flux linkage associated
with the coil [22]. Variations in the electrical conductivity or the presence of flaws or
inclusions will cause a change in the eddy current flow or equivalently will cause an
increase in the apparent resistance of the coil.

In most ferrous steel products, eddy current testing is limited to surface examination
due to the relatively high permeability of these materials.
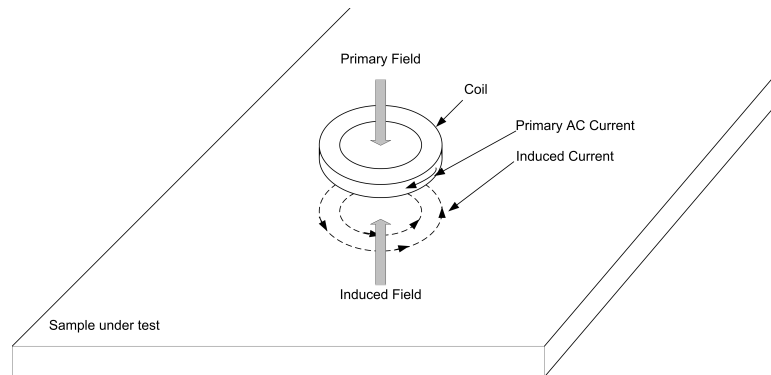
Figure 1.6: Eddy current testing.

Ultrasonic Testing

Ultrasonic Testing (UT) uses sound waves to conduct examinations and make mea-
surements. Ultrasonic inspection can be used for flaw detection, dimensional mea-
surements, material characterization, and a multitude of other applications.

Figure 1.7 illustrates a typical pulse/echo UT inspection system: it consists of several
functional units including a pulser/receiver, transducer, and display devices. The
pulser/receiver produces a high-voltage electrical pulse to drive the ultrasonic trans-
ducer. Driven by the pulser, the transducer generates high frequency ultrasonic energy
(typically in the range from 1-10MHz). The sound wave is introduced to the sample

under test and propagates through its bulk until a discontinuity (such as a crack) is encountered in the wave path. At the discontinuity portion of the energy will be reflected back to the transducer. The reflected wave signal is transformed into an electrical signal by the transducer. The signal travel time can be directly related to the distance that the signal propagated. From the signal, information about the reflector location, size, orientation and other features can be inferred.
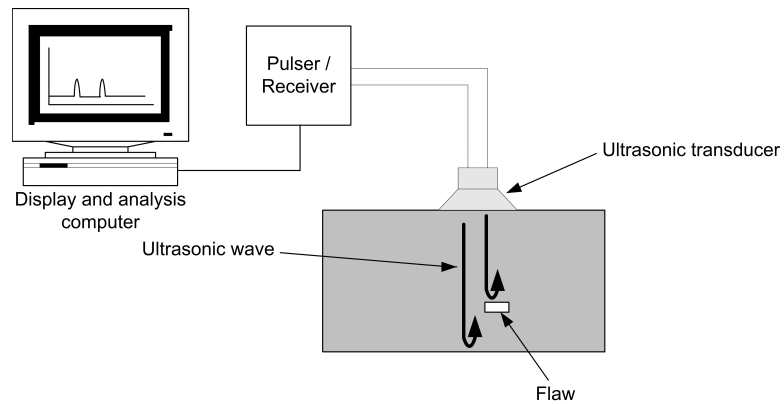
Figure 1.7: Ultrasonic pitch/catch test arrangement.

X-Ray Imaging

X-ray inspection or radioscopy is based on the absorption of X-rays by the sample under test. It uses an X-ray tube to emit a beam of ionizing radiation. The radiation passes through the part being inspected and impinges on the imaging device as shown in Figure 1.8.

As the beam travels through the sample, the X-ray energy is attenuated in proportion to the material thickness. The presence of flaws, inclusions or pores will cause a reduction in the attenuation. The imaging device includes an image intensifier that produces a high resolution image that displays the attenuation level.
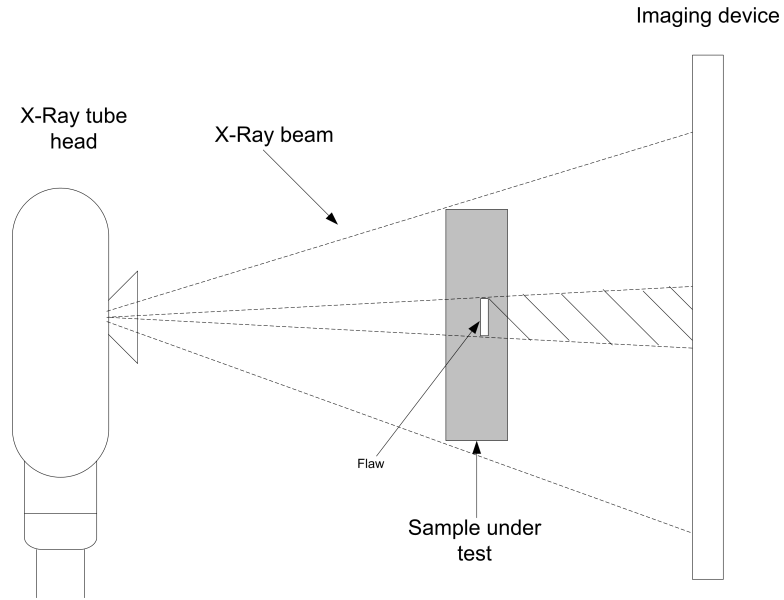
Figure 1.8: X-ray testing with a radiation source.

Resonance Testing

Resonant inspection is conducted by exciting a sample with low frequency harmonic elastic waves over a certain bandwidth. The measurement then records the resonance frequency response via separate transducers operating as receivers as shown in Figure 1.9.

Any abnormalities encoutered in a defective part will result in shifts of the resonance spectra. Therefore, the resonance technique compared the spectral response of an unflawed part with the shifted spectral response of a flawed part.
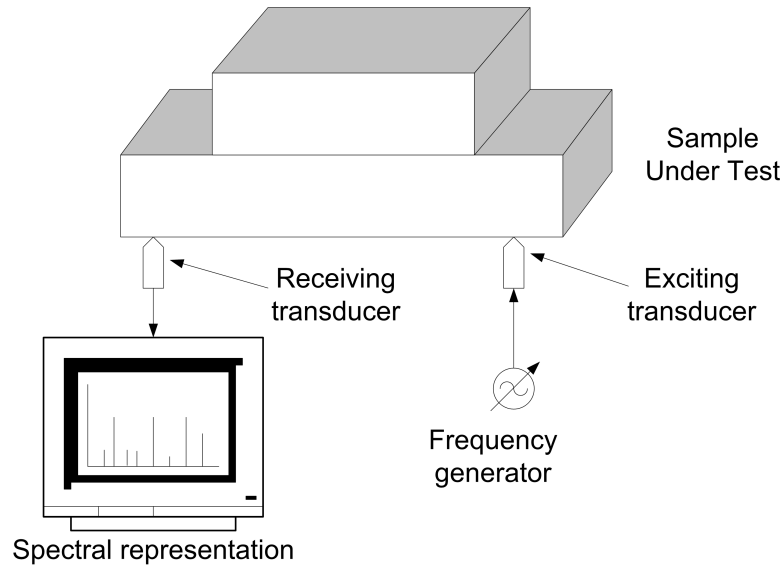
Figure 1.9: Basic resonance test arrangement. A wideband transducer generates a spectrum of resonances that is recorded by a second receiving transducer.

Electrical Resistivity

The traditional electrical resistivity inspection method illustrated in Figure 1.10 utilizes four in-line probes to measure the resistance of the material in the area of interest. The outer probes are used to feed current into the sample under test and the inner probes measure the voltage drop across them. The benefit of this method over a simple two wire method is that the voltage is measured next to the current carrying leads. This eliminates the lead resistance effect [4] . The accuracy of this method depends mainly on the ability to precisely record the voltage drop for a given current.
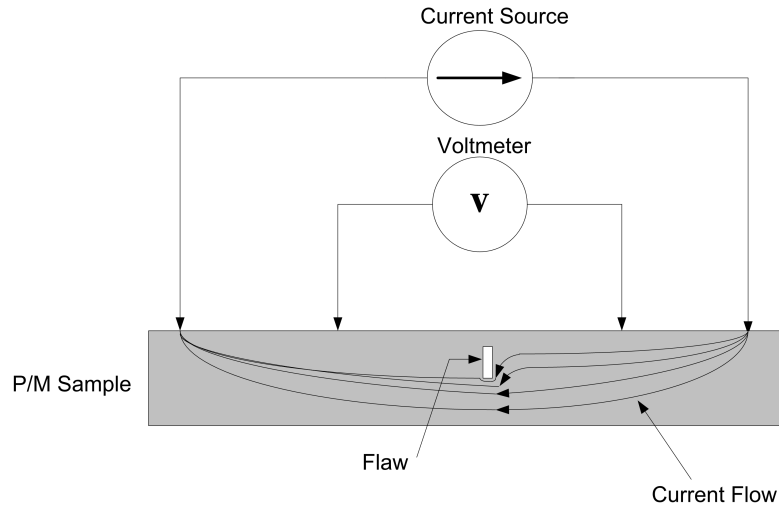
Figure 1.10: Four-probe resistivity measurement setup.

In P/M compacts, material properties can be inferred from the conductivity of the material [1]. The technique has been successful in the detection of surface and near-surface defects. However, it suffers from two main drawbacks. First, the coverage of the sensor is very limited. Therefore, a complete test requires indexing the probe across the entire surface of the sample. Second, conflicting requirements might arise between resolution and the ability to detect deep subsurface flaws, where the spacing between the probes is the determining factor. The resolution is increased by reducing the spacing between the probes and the depth of detection is improved by increasing the spacing [1].

To overcome these limitations an apparatus for crack detection in green-state P/M compacts was developed at Worcester Polytechnic Institute [4, 1]. This apparatus uses a technique that is an extension of the basic resistivity measurement principles where, a multi-probe sensor shown in Figure 1.11 is used. Here a multiple current injection pattern based on the plurality of the current probes is utilized in conjunction with a large number of probes covering the entire area of the sample under test. The system enables the measurement of the voltage distribution over a large surface area.

It enhances the ability of the apparatus to detect both small surface cracks and deep subsurface defects.
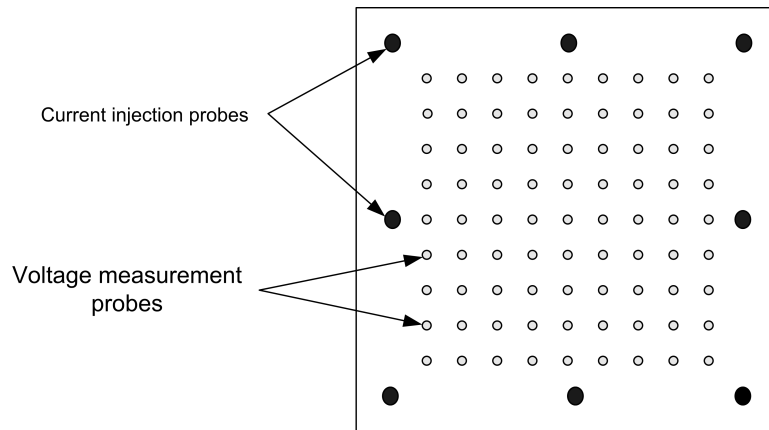
Figure 1.11: Multi-pin planar sensor.

1.2.2 Comparative Study

After introducing the main NDE techniques used in P/M and in most metal working techniques and processes, it is necessary to comparatively review these methodologies with regards to their relative strengths and weaknesses. When considering the basic steps in the P/M manufacturing cycle of mixing, compacting and sintering, it becomes apparent that the compaction step offers the highest cost efficiency. consequently special emphasis will be placed on the usability of each technique in the testing of green-state parts. Table1.1 lists the most widely employed NDE techniques and highlights their relative capabilities and limitations with respect to testing green-state samples.

Table 1.1: Advantages and disadvantages of various NDE techniques applied to P/M inspection.

Technique	Capabilities	Limitations
Resistivity	• Demonstrated performance with green state parts • Requires sensor adjustment to compact	• Complex test set-up • Generally does not work for sintered parts
Eddy current	• Ideal for surface and near surface defects in sintered parts • Coil sensor can be adjusted to fit the part	• Depth of penetration limits the usability in green-state to surface detection
Resonance	• Simple test method for complex, sintered parts	• Cannot provide individual flaw signatures • Scientifically unproven in P/M compacts
Ultrasonics	• Can detect deeply embedded defects in sintered parts • Cost effective • Easy to set up	• Inefficient in green-state due to high acoustic attenuation • Requires a coupling agent (usually a viscous gel)
X-Ray	• Detects defects in both green state and sintered • High resolution and deep penetration • Established technology for high quality samples (aerospace and military)	• Not suitable for high volume applications (slow) • High ownership cost • Not effective in detecting near corner defects

As can be deduced, there appears to be no single technique that can effectively be applied to green-state part inspection.

1.3   Research Objective

Goal of this research effort is the design of a new thermo-electric testing methodology for green-state and sintered compacts. We intend to modify and extend the previously developed electrostatic testing methodology in such a way as to use the direct current electric excitation to create Joule heating in the compact. The resulting temperature distribution emanating from the sample can then be detected in the IR spectrum through an infrared camera. Our proposed thermo-electric solution will attempt to overcome the limitations associated with the previously discussed approaches. In particular, it is expected that no special sensor development will be required. Furthermore, the technique is expected to equally apply to green-state and sintered compacts. This new technique is considered a global area inspection method in that it allows the detection and measurement of absolute temperatures and temperature differences over large surfaces.

We intend to use DC current as heating source (Joule heating). As a result, due to the finite conductivity of the compacts a power loss is created. Based on the laws of thermodynamics the power loss translates into thermal stimulation that can be recorded as IR radiation emanating from the compact.

In an effort to extend the IR detection scheme we intend to explore dynamic testing, known as pulsed thermography whereby the sample is excited with a current pulse and the thermal response is recorded over time. This will enhance our detection capabilities to include subsurface defects and relatively small surface breaks.

1.4 Approach

The overall research is organized as shown in Figure 1.12. Specifically, the electric power deposition is determined through the use of an electrostatic model where the conductivity is calculated from density information through an inverse algorithm as developed in the previous research effort. The temperature distribution on the surface of the part can subsequently be detected through an IR camera.
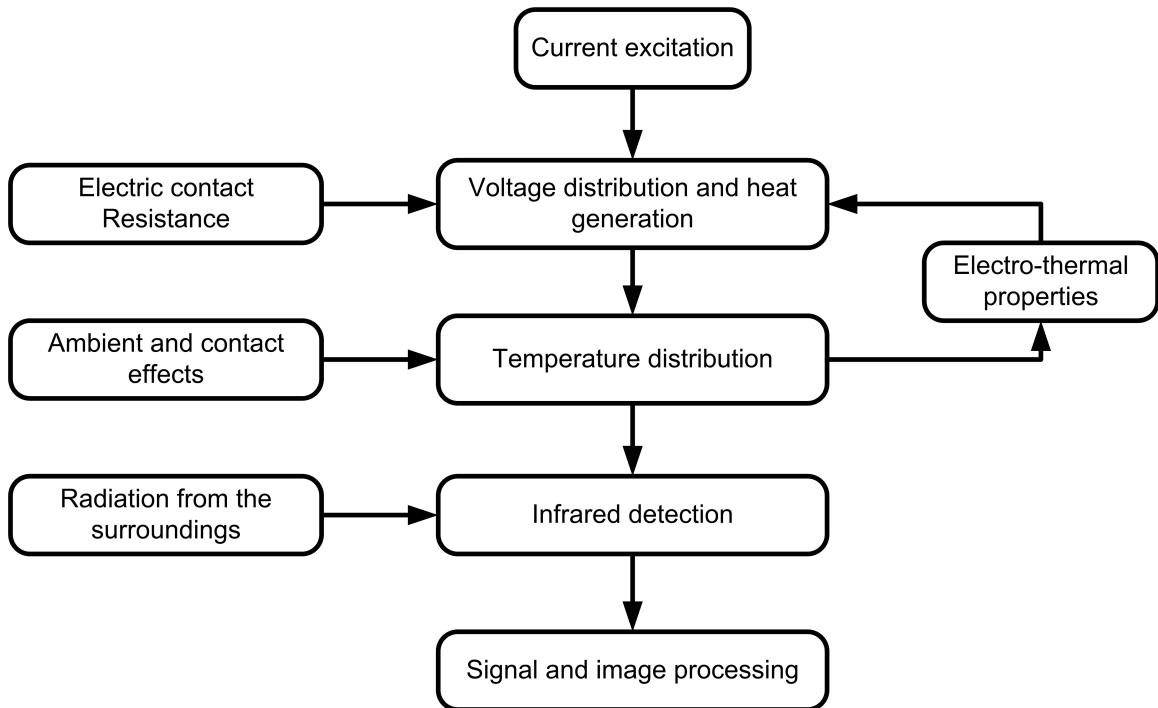
Figure 1.12: Block diagram of overall testing approach.

The devised approach includes the development of the necessary theoretical modeling tools. The study will investigate the forward solution, i.e. we will study the energy transfer mechanisms between the electrical and thermal models. This effort will concentrate on:

- Current propagation and potential differences in the part (electrostatics).

- Temperature distribution (heat transfer).

- IR radiation and detection.

In addition, due to the complex and multi-disciplinary nature of the thermo-electric phenomena, numerical modeling will be extensively used to study the thermal response of perfect and flawed samples subject to electric excitation. The first phase will involve a steady state approach, followed by a more elaborate transient analysis.

Performance evaluation focuses on testing controlled samples with different material compositions, different flaw sizes, depths and orientations. This evaluation will explore the accuracy of the method and its sensitivity.

1.5 Thesis Organization

This chapter introduced the basic steps in the P/M manufacturing process; it discussed the quality challenges and requirements the industry is facing and it discussed the most widely used NDE techniques. We also outlined in this chapter the goal of our research and state its purpose and the approach taken.

Chapter 2 will be devoted to the theoretical foundation of the detection system. It will include a study of the current flow in a simple geometry. Here an analytical solution to Laplace's equation will be derived. Similarly an analytical solution to the simplified heat equation will be derived. Finally, we will conclude this chapter with a comprehensive discussion of the principles of heat radiation.

In Chapter 3 the numerical model based on the finite element method (FEM) will be discussed. This model is needed to solve the electrostatic Laplace's equation. Next, another FEM model will simulate the heat equation in terms of predicting the temperature distribution on the surface of the compact. This modeling approach will be sufficiently flexible to handle both the static and the dynamic heat transfer phenomena.

Chapter 4 is dedicated to experimental results, and a discussion of the outcome. IR images of simple and complex P/M parts will be shown to validate the technique. First, simple flawed and unflawed parts are tested and results are presented, followed by more generalized results of complex green-state and sintered parts.

Finally, Chapter 5 summarizes the thesis, draws conclusions from the theoretical formulation, simulation and experimentation. It will contain also suggestions and recommendations for future work.

Chapter 2

Theoretical Formulation

2.1 Introduction

Since the proposed research employs DC current to cause the temperature of the part
to rise (Joule heating), the flow of current is governed by the laws of electrostatics.
However, consistent with the laws of thermodynamics, the power loss can be recorded
as IR radiation emanating from the compact.

Therefore, to develop a full and comprehensive theoretical model of the IR inspection
system, we are studying three separate physical models: electrostatics, thermal, and
radiation. Specifically we have to isolate the following parameters:

- the electric heat source, including the electro-thermal coupling,

- the heat distribution over the surface, including mechanisms that take into
  account ambient effects, and

- the IR imaging system that records all sources of radiation as well as optical
  effects due to the camera and due to the relatively small emissivity of the P/M
  parts.

The following sections discuss in more detail the mathematical steps involved in the model formulation.

2.2 Heat Source

Electric energy is coupled into the P/M sample through surface contacts. This energy is in a form of direct current (DC), which will establish a voltage distribution throughout the part. The potential difference across the length of the part is equal to the work per unit charge required to move the charge through the length [19]. The relation illustrated in (2.1) is the basic idea underlying Joule's law :

$$\frac{Work}{Charge} * \frac{Charge}{Time} = \frac{Work}{Time} = Power \tag{2.1}$$

Equation (2.1) shows the power dissipated in the length of the conducting part.

Ohm's law, however, suggests that a constant of proportionality exists between the current injected I and the potential difference V across the length d of the sample. This constant is what is called resistance R, it can be expressed as:

$$R = \frac{V}{I} = \frac{-\int \mathbf{E} \cdot d\mathbf{l}}{\int\int \mathbf{E} \cdot d\mathbf{S}} \tag{2.2}$$

or as commonly known:

$$V = I\mathbf{R} \tag{2.3}$$

Equations (2.1) and (2.2) imply that the power dissipated in the conductor can be written as:

$$P = VI = I^2\mathbf{R} \tag{2.4}$$

Applying a constant voltage to a P/M compact can be accomplished through inserting

the latter between two large contacts as shown in Figure 2.1. The purpose of these large contacts is to reduce boundary effects due to charge build up and to ensure uniform current flow into the part.
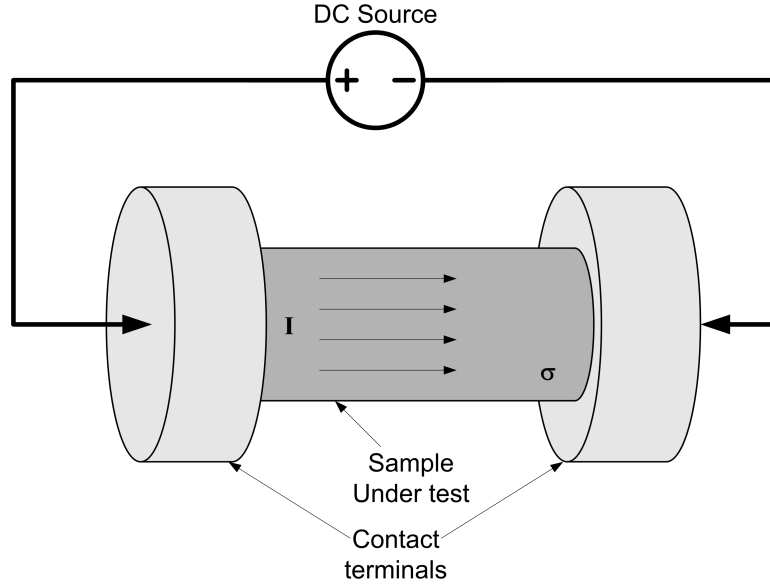
Figure 2.1: Cylindrical P/M part placed between end blocks.

Ohm's law in its current form represents a simplified view where it assumes uniform conductivity and a constant resistance. This simplified view can no longer hold when applied to parts such as green-state P/M compacts due to their amorphous nature and non-uniform density distribution. Also when detecting defects on the order of 20 μm, small voltage drops associated with the contact resistance can no longer be neglected.

The more generalized view takes into account the spatial dependency of the conductivity of the part and the voltage along its length. This approach uses Laplace's equation in the form:

$$\nabla \cdot (\sigma \nabla V) = 0 \tag{2.5}$$

Here $\sigma(x, y, z)$ is the electric conductivity of the medium and $V(x, y, z)$ is the voltage

distribution in the sample.

This equation is a second order partial differential equation (PDE) that can be solved analytically for canonical geometries. A number of different solution methods have been developed, most notably the separation of variables, Fourier series, or Laplace transformation [17]. For simplicity, we chose the method of separation of variables in cylindrical coordinates.

In this system, where r, θ, and z are the independent variables, (2.5) can be cast as

$$\frac{\partial^2 V}{\partial r^2} + \frac{1}{r}\frac{\partial V}{\partial r} + \frac{1}{r^2}\frac{\partial V}{\partial \theta^2} + \frac{\partial^2 V}{\partial z^2} = 0 \tag{2.6}$$

The separation of variables technique suggests a solution of the form:

$$V(r,\theta,z) = \mathcal{R}(r)\,\Theta(\theta)\,Z(z) \tag{2.7}$$

When V is substituted in (2.6) , we obtain

$$\frac{Z\Theta}{r}\frac{d}{dr}\left(r\frac{d\mathcal{R}}{dr}\right) + \frac{\mathcal{R}Z}{r^2}\frac{d^2\Theta}{d\theta^2} + \mathcal{R}\Theta\frac{d^2Z}{dz^2} = 0 \tag{2.8}$$

Dividing by $V = \mathcal{R}\Theta Z$ yields

$$\frac{1}{\mathcal{R}r}\frac{d}{dr}\left(r\frac{d\mathcal{R}}{dr}\right) + \frac{1}{r^2\Theta}\frac{d^2\Theta}{d\theta^2} + \frac{1}{Z}\frac{d^2Z}{dz^2} = 0 \tag{2.9}$$

Equation (2.9) can be separated into two ordinary differential equations (ODEs):

$$\begin{cases} \dfrac{1}{Z}\dfrac{d^2Z}{dz^2} = -\gamma^2 \\[4mm] \dfrac{1}{\mathcal{R}r}\dfrac{d}{dr}\left(r\dfrac{d\mathcal{R}}{dr}\right) + \dfrac{1}{r^2\Theta}\dfrac{d\Theta}{d\theta} = \gamma^2 \end{cases} \tag{2.10}$$

The second term in (2.10) can also be separated into two separate ODEs , resulting in the following equations :

$$\frac{d^2Z}{dz^2} + \gamma^2 Z = 0 \tag{2.11}$$

$$\frac{d\Theta}{d\theta} + \beta^2 \Theta = 0 \tag{2.12}$$

$$\frac{d^2\mathcal{R}}{dr^2} + \frac{1}{r}\frac{d\mathcal{R}}{dr} - (\gamma^2 + \frac{\beta^2}{r^2})\mathcal{R} = 0 \tag{2.13}$$

Here γ and β are arbitrary separation constants.

The solution to (2.11) takes the form:

$$Z(z) = C_1 \cosh \gamma z + C_2 \sinh \gamma z \tag{2.14}$$

and similarly the solution to (2.12) is:

$$\Theta(\theta) = B_1 \cos \beta \theta + B_2 \sin \beta \theta \tag{2.15}$$

We observe that by introducing another variable α such that

$$\alpha^2 + \gamma^2 = 0 \tag{2.16}$$

equation (2.13) takes the form of a Bessel's equation. Its general solution is:

$$\mathcal{R}(r) = A_1 J_n(\alpha r) + A_2 Y_n(\alpha r) \tag{2.17}$$

where J_n is the Bessel function of the first kind of order n and Y_n is the nth-order Bessel function of the second kind .

In equations (2.14) - (2.17) A_1, A_2, B_1, B_2, C_1 and C_2 are integration constants.

The finale solution of Laplace's equation will therefore be:

$$
\begin{aligned}
V(r,\theta,z) \;=\; & [C_1\cosh\gamma z + C_2\sinh\gamma z]\,[B_1\cos\beta\theta + B_2\sin\beta\theta] \\
& \cdot\; [A_1 J_n(\alpha r) + A_2 Y_n(\alpha r)] \tag{2.18}
\end{aligned}
$$

If one considers the solid cylinder illustrated in Figure 2.1 with a uniform density, (2.18) can be substantially simplified.

Specifically, the electric potential will be independent of θ due to symmetry. The solution of (2.6) takes on the form

$$
V(r,z) = [A\cosh\gamma z + B\sinh\gamma z]\,J_0(\alpha r) \tag{2.19}
$$

The associated boundary conditions involve the inward pointing surface normal $\mathbf{n}$ and the current density $\mathbf{J}$. This allows us to specify the electric flux

$$
\mathbf{n}\cdot(\sigma\nabla V) = -\mathbf{n}\cdot\mathbf{J} \tag{2.20}
$$

All remaining boundaries, excluding the ground connection, are set to be insulating or flux free

$$
\mathbf{n}\cdot\mathbf{J} = 0 \tag{2.21}
$$

The imposed boundary conditions yield a special case of the Sturm-Liouville system, with eigenfunctions of the form

$$
V(r,z) = \sum_{n=1}^{\infty} A_n J_0(\gamma_n r)\sinh(\gamma_n z) \tag{2.22}
$$

Here γ_n's are the positive roots of the Bessel function of the zeroth order

$$
J_0(\gamma_n R) = 0,\quad n = 1, 2, 3, \dots. \tag{2.23}
$$

Now we need to determine the coefficients A_n in (2.22) in such away that $V(r,L) = f(r)$. Here $f(r)$ is an arbitrary function of r that can be expanded so as to satisfy the boundary condition.

We make use the orthogonality of Bessel functions to write a Fourier-Bessel expansion of $f(r)$ over the interval $(0,R)$ at $z = L$.

$$f(r) = \sum_{n=1}^{\infty} A_n \sinh(\gamma_n L) J_0(\gamma_n r) \tag{2.24}$$

The coefficients A_n may readily be obtained as

$$A_n = \frac{\int_0^R f(r) J_0(\gamma_n r) r dr}{\int_0^R J_0^2(\gamma_n r) r dr} \tag{2.25}$$

Using the following identification

$$\frac{d}{dr}[r J_1(\gamma_n r)] = \gamma_n r J_0(\gamma_n r) \tag{2.26}$$

Integrating through, will result in

$$\int_0^R J_0(\gamma_n r) r dr = \frac{R}{\gamma_n} J_1(\gamma_n R) \tag{2.27}$$

Therefore the formulation can be simplified to

$$A_n = \frac{2}{R^2 J_1^2(\gamma_n R)} \int_0^R f(r) J_0(\gamma_n r) r dr \tag{2.28}$$

For this particular case, $f(r) = V_0$ is a constant. The solution becomes

$$V(r,z) = \frac{2V_0}{R} \sum_{n=1}^{\infty} \frac{J_0(\gamma_n r) \sinh(\gamma_n z)}{\gamma_n J_1(\gamma_n R) \sinh(\gamma_n L)} \tag{2.29}$$

A solution is plotted in Figure 2.2 , involving the parameters $R = 0.01m$ and $L = 0.06m$.
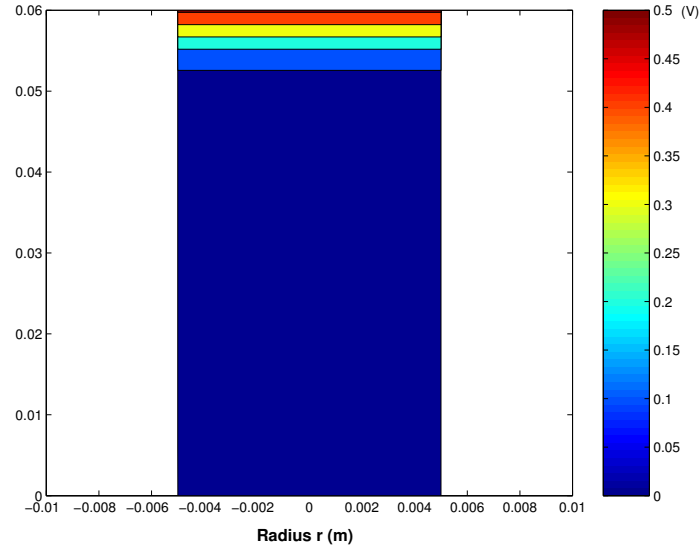
Figure 2.2: Voltage distribution in a cylindrical compact.

The electric current flowing through the compact will create a voltage distribution and deposit power (Joule heating) due to the finite conductivity in the sample. The power per unit volume Q is described by the following equation

$$Q = \frac{J^2}{\sigma} = \sigma E^2 = \sigma \left| \nabla V^2 \right| \tag{2.30}$$

where E is magnitude of the electric field.

The deposited electrostatic power will cause the temperature of the part to rise gradually until it reaches equilibrium (known as the Joule effect). This process is influenced by the thermal properties of the part and the atmospheric conditions (ambient temperature).

2.3 Temperature Distribution

The science of heat transfer allows us to predict the temperature distribution and heat exchanges in the system. Heat exchange between bodies is governed by three mechanisms: conduction (within solids), convection (between the surface of a solid and a moving fluid such as air), and radiation (between two solids). The following sections will introduce these principles with an emphasis on both conduction and radiation as they constitute the main heat transfer mechanism and foundation of the thermal detection.

2.3.1 Heat Conduction

The mechanism of heat conduction on the molecular level refers to the exchange of kinetic energy between the micro-particles in the high and low temperature regions [10]. The heat conduction on the macroscopic scale, however, disregards the molecular structure of the medium and treats it as a continuum.

Heat transfer processes are quantified in terms of the appropriate rate equations. The rate equation in heat conduction is known as *Fourier's Law.*

The unidimensional and steady state form is illustrated in (2.31), and an example is shown in Figure 2.3 where q_x is the rate of heat transferred by conduction through the finite surface A_x.

$$q_x = -kA_x \frac{dT}{dx} \tag{2.31}$$

Here A_x is a surface perpendicular to the heat transfer direction, k is the thermal conductivity $(W/m\,°C)$, and T is the temperature. Here the negative sign is a consequence of the second law of thermodynamics, which indicates that energy is transfered from the high temperature point to the low.
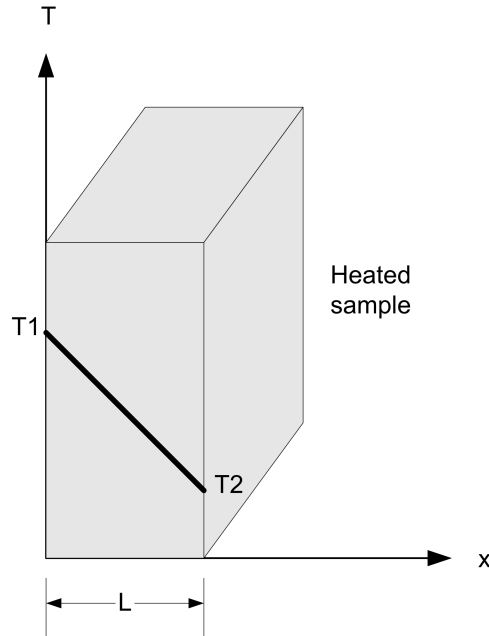
Figure 2.3: One-dimensional conduction heat transfer.

Equation (2.31) is not an equation that can be derived from first principles, but rather is a generalization based on experimental evidence [11]. It defines, however, one of the most important material properties: the thermal conductivity k (which represents the conduction rate of the medium per unit area and for a temperature gradient of $1\,°C$). This parameter will be the center of our attention when modeling and testing P/M parts. In general sintered parts have a high thermal conductivity comparable to iron steel and green-state parts.

Our analytical investigation will extend to the derivation of a generalized heat conduction equation that will include transient effects.

To do so we consider a stationary, isotropic and opaque solid. The transient multi-dimensional equation is written

$$\rho c \frac{\partial T}{\partial t} - \nabla \cdot (k \nabla T) = Q \tag{2.32}$$

where the parameters in (2.32) are the density of the material ρ in kg/m^3 , heat capacity c in $W/kg\,°C$, thermal conductivity k in $W/m\,°C$, and heating power Q in W/m^3.

2.3.2   Heat Convection

In convection heat transfer mechanism, heat is transferred from a surface by a moving fluid. This is a cumulative process, where energy transfer is due to a random molecular motion (diffusion) and a macroscopic motion of the fluid [11]. A consequence of the fluid-surface interaction is the development of a hydrodynamic region or boundary layer of fluid through which the velocity of the latter varies from zero at the surface to a finite value associated with the flow as shown in Figure 2.4.
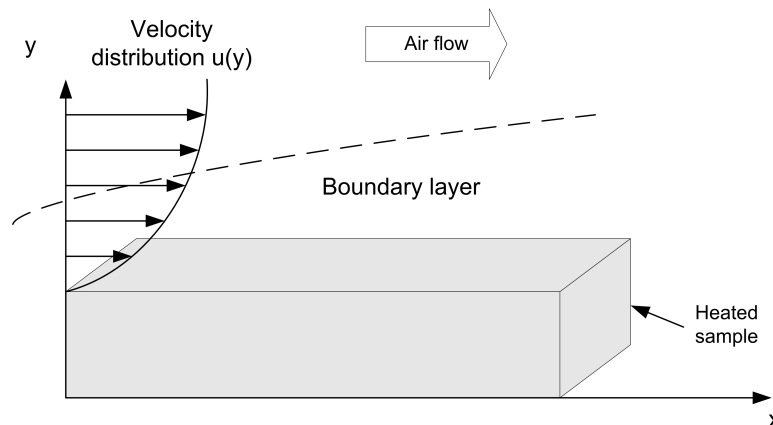
Figure 2.4: Convection heat transfer and development of a boundary layer.

Convection heat transfer is classified according to the nature of the flow. In free (natural) convection the flow is induced by buoyancy forces caused by temperature variations in the fluid. In forced convection the surface is subjected to a flow caused by external means such as fans or pumps.

The derivation of an analysis model for convection requires the study of mass, momentum, energy laws and the laws of viscous shear. However a simple model to compute

the heat transfer rate can be cast in the form

$$q_c = hA_s \left(T_S - T_F \right) \tag{2.33}$$

where q_c is the heat transfer rate from a surface A_S at a temperature T_S, T_F is the fluid temperature and h is the average convective heat transfer coefficient in $W/m^2\,{}^\circ C$. This coefficient encompasses all the parameters that influence convection. It depends on conditions in the boundary layer, which are influenced by surface geometry, the fluid flow, and other fluid thermodynamics and transport properties [11].

2.3.3   Radiation

The mechanism of heat emission is related to the energy released as a result of oscillations or transitions of the electron energy states that constitute the medium. These oscillations, are in turn, sustained by the internal energy which is determined by the temperature of the medium [23].

As we know, all forms of matter emit thermal radiation; it is a volumetric phenomenon. However, in P/M parts, due to the fact that they are solids, it becomes a surface effect because the radiation emitted by interior molecules is strongly absorbed by adjoining ones. Thus, the thermal radiation is limited to the molecular layers that are either on the surface or at approximately $1\mu m$ below the surface.

This thermal transfer mechanism can be viewed as propagation of electromagnetic waves of a range of wavelengths. Similar to an antenna system, the directionality of the radiation becomes very important as depicted in Figure 2.5. For this reason, it is necessary to study both the spectral distribution and the directional distribution of the radiation in order to accurately determine the energy and the temperature of a heated P/M part.
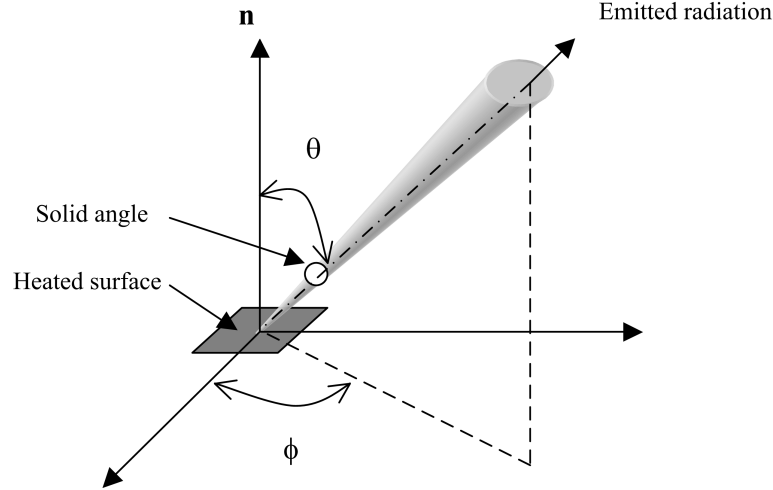
Figure 2.5: Directional nature of infrared radiation emanating from a heated surface element.

The rate at which radiated energy is emitted at a wavelength in a specific direction is a function of the area of the emitting surface normal to the direction, the solid angle, and the spectral interval. It is referred to as the *spectral intensity*

$$L_{\lambda,e}(\lambda,\theta,\phi) = \frac{dq}{dA_1 \cos\theta \, d\Omega \, d\lambda} \tag{2.34}$$

By integrating this entity (the spectral radiance) over a finite angle and a finite wavelength we find the radiant power, also called the *spectral exitance*. For a Lambertian surface (isotropically diffuse) the exitance $M(\lambda)$ is:

$$M(\lambda) = \pi L(\lambda) \tag{2.35}$$

A spatial integration on the other hand, will result in the *spectral hemispherical emissive power* $E_\lambda \left(W/m^2 \mu m\right)$, which quantifies the rate at which radiation is emitted in all directions from a surface per unit wavelength and per unit area. This quantity is

regarded as a flux emanating from the area of the compact and is expressed as follow

$$E_\lambda(\lambda) = \int_0^{2\pi} \int_0^{\frac{\pi}{2}} L_{\lambda,e}(\lambda, \theta, \phi) \cos\theta \sin\theta \, d\theta \, d\phi \qquad (2.36)$$

To quantify the total emissive power E_e one has to consider all possible wavelengths, and all possible directions as depicted in the following integral

$$E_e = \int_0^{\infty} E_\lambda(\lambda) \, d\lambda \qquad (2.37)$$

A qualitative analysis of radiation effects often uses a baseline. Namely, a gold standard to reference all radiation parameters, and to be used as a baseline for subsequent measurements. This object has the property of being the perfect emitter and the perfect absorber at the same time [11]. Emissions emanating from this object are independent of direction and wavelength. This object is called the *blackbody* and its spectral radiance is given by Planck's law

$$L_{\lambda,b}(\lambda, T) = \frac{c_1}{\pi\lambda^5 \left[\exp\left(\frac{c_2}{\lambda T}\right) - 1\right]} \qquad (2.38)$$

Here T is the temperature of the target in Kelvin, and c_1 and c_2 are constants. This equation yields a set of graphs known as the blackbody emissivity power. We find for P/M samples at the temperature of interest that the peak radiation occurs between $7\mu m$ to $15\mu m$, as shown in Figure 2.6.
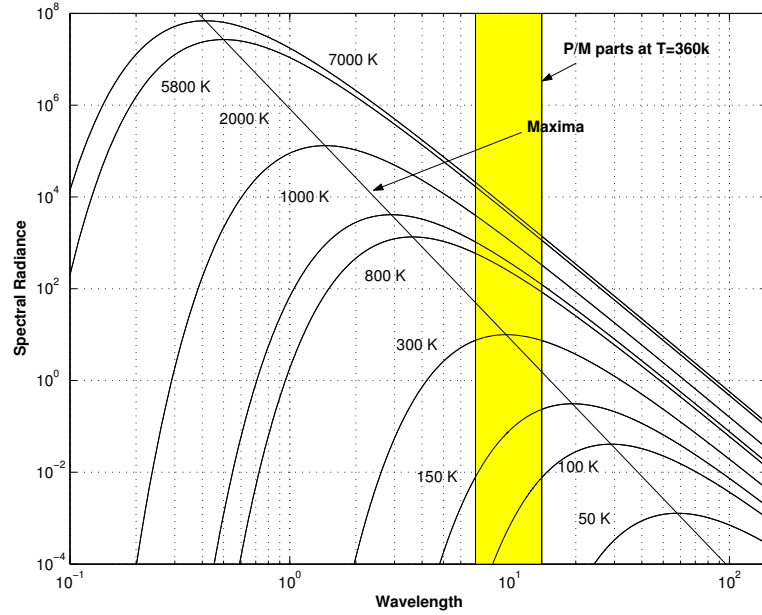
Figure 2.6: Black body radiation spectrum.

From these graphs we determine the locus of the maximum spectral radiance for a given temperature by derivating Planck's law. From the derivation we obtain the following expression

$$\lambda_{max} = \frac{c_3}{T} = \frac{2897.7}{T} \tag{2.39}$$

where c_3 is the third radiation constant.

A simpler approach to calculate the amount of radiation in all directions and across all wavelengths will be based on Stefan-Boltzmann's law. Here temperature is the only parameter needed as given in the following expression

$$E_b = \sigma T^4 \tag{2.40}$$

σ is the Stefan-Boltzmann constant. It has the numerical value $\sigma = 5.670 \times 10^{-8} W/m^{2}{}^{\circ}K^4$.

Unfortunately, a real surface is neither a perfect emitter nor a perfect absorber. We therefore define an additional surface property to express the ability of a body to emit

energy. This property is used as a correction factor and is called emissivity *e*. It is a unitless factor that spans from 0 for a total reflector to 1 for a blackbody. The emissivity depend on several spectral, spatial and material parameters. Emissivity is of major concern in IR imaging due to the fact that the radiance and hence temperature is directly proportional to the emissivity as illustrated in (2.41) . For example for a surface having a spectral emissivity $e(\lambda)$, the radiance is expressed as:

$$L_{\lambda,e(\lambda)}(\lambda, T) = e(\lambda) L_{\lambda,b}(\lambda, T) \tag{2.41}$$

Metals in general, as well as P/M samples, posses a low emissivity. This makes accurate IR radiometry very challenging and in some cases impossible. Furthermore, the thermal dependency of the emissivity greatly limits the applicability of IR thermography. However, all these shortcomings can be overcome with a judicious choice of the temperature at which the measurement is conducted.

2.3.4 Combined Heat Transfer Applied To P/M Samples

In general, the thermal behavior of a body is described by the generalized heat equation

$$\rho c \frac{\partial T}{\partial t} - \nabla \cdot (k \nabla T) = Q - h(T - T_{ext}) - C\left(T^4 - T_{amb}^4\right) \tag{2.42}$$

The dominant transfer mechanism in our proposed testing technique is heat conduction. We therefore obtain the simplified expression, illustrated in (2.32). This equation is a second order PDE that can be solved following the same steps described to solve Laplace's equation. In this formulation it is assumed that the sample surface is cooled through natural convection, implying a Neumann type boundary condition

$$\mathbf{n} \cdot (k \nabla T) = h(T_{ext} - T) \tag{2.43}$$

Here T and T_{ext} are sample temperature and external temperature, respectively.

Therefore, in the cylindrical coordinate system we will write the axis-symmetric relation

$$\frac{k}{r}\frac{\partial}{\partial r}\left(r\frac{\partial T}{\partial r}\right) + \frac{\partial^2 T}{\partial z^2} = \rho c\frac{\partial T}{\partial t} - Q \tag{2.44}$$

where the temperature and the power deposited are function of only r, z and t .

Under steady state condition (2.44) simplifies to

$$\frac{k}{r}\frac{\partial}{\partial r}\left(r\frac{\partial T}{\partial r}\right) + \frac{\partial^2 T}{\partial z^2} = -Q \tag{2.45}$$

Here is a base temperature specified as a function of radius and the boundary conditions

$$k\frac{\partial T\,(R,z)}{\partial r} + hT\,(R,z) = 0 \tag{2.46}$$

$$k\frac{\partial T\,(r,L)}{\partial r} + hT\,(r,L) = 0 \tag{2.47}$$

$$k\frac{\partial T\,(r,0)}{\partial r} + hT\,(r,0) = 0 \tag{2.48}$$

The axis-symmetric solution can be developed in an orthogonal series expansion of the form

$$T\,(r,z) = \frac{2QhR^3}{k}\sum_{n=1}^{\infty}\frac{1 - \dfrac{(hR/\gamma_n)\cosh\,(\gamma_n z/R)}{[\tan\,(\gamma_n L/R) + hR/\gamma_n] + \cosh\,(\gamma_n L/R)}}{\left[1 + (hR/\gamma_n)^2\right]\gamma_n^A J_0\,(\gamma_n)}J_0\left(\frac{\gamma_n r}{R}\right) \tag{2.49}$$

In (2.49) γ_n are the positive roots of the transcendental equation:

$$\gamma J_1\,(\gamma_n) = RhJ_0\,(\gamma_n) \tag{2.50}$$

An example solution was computed for the following numerical parameters representing a green-state P/M compact:

- Radius: $R = 0.01\,m$

- Length: $2L = 0.06\,m$

- Heating Power: $Q = 767\,kW/m^3$

- Thermal conductivity: $k = 25\,W/m\,^\circ C$

- Convection heat transfer coefficient: $h = 10\,W/m^2\,^\circ C$

Figure 2.7 illustrates the temperature distribution throughout the compact. As expected, the temperature is at a maximum at $r = z = 0$ and begins to decay to a minimum value at the surface due to the convective boundary.
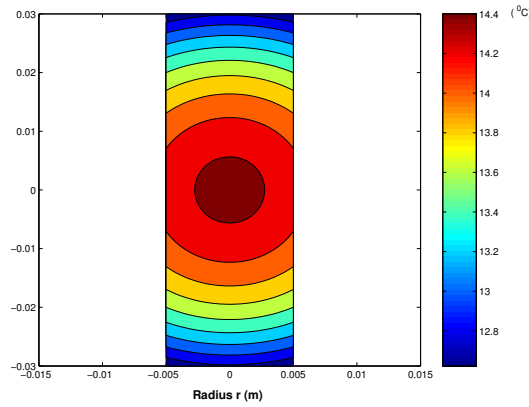
Figure 2.7: Temperature distribution for a cylindrical compact. Dimensions are recorded in m.

A time varying solution in r and t with the initial condition

$$T(r,0) = T(r) - T_0 \tag{2.51}$$

can be derived as follow

$$T(r,t) = \frac{2QhR^2}{k}\left[\frac{1}{8}\left(1 - \frac{r^2}{R^2}\right) + \frac{1}{4Rh} - Rh\sum_{n=1}^{\infty} \frac{e^{-\gamma^2\tau/R^2}J_0\left(\frac{\gamma_n r}{R}\right)}{\left[1 + (hR/\gamma_n)^2\right]\gamma_n^4 J_0(\gamma_n)}\right] \tag{2.52}$$

where

$$\tau = \frac{kt}{\rho c} \tag{2.53}$$

The solutions (2.49) and (2.52) can be used as benchmarks to verify both the modeling and the experimental results.

2.4 Infrared Detection

Our thermal system does not measure the temperature directly, but rather it records the radiant flux received by the imager from an area of interest subtending the solid angle at the camera, weighted by the imager's spectral response.

In general, the radiation stems from three sources: the radiation coming directly from the sample, the radiation incident and reflected from the sample, and the radiation emitted by the atmosphere . Therefore, we write the radiation with its three components (see Figure 2.8) as a sum

$$S = S_s + S_r + S_{at} \tag{2.54}$$
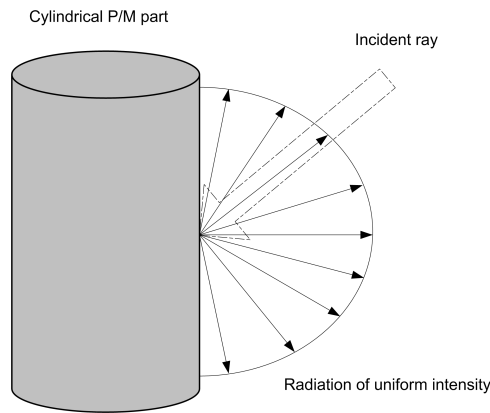
Figure 2.8: Radiation and reflection from a point on the surface of a P/M part.

Specifically the component arising from the radiation emitted by the sample is given

by

$$S_s = K \int_0^\infty L\left(\lambda\right) A_{at} R(\lambda) d\lambda \tag{2.55}$$

Here λ is the wavelength, $L\left(\lambda\right)$ is the spectral radiance of the sample, A_{at} is the spectral transmission of the atmosphere, and $R\left(\lambda\right)$ is the effective spectral responsivity of the imager's detector (transmission of the lens and any additional elements in the optical path).

Similarly, we can derive the radiation reflected from the sample and the radiation emitted by the atmosphere between the camera and the sample.

$$S_r = K \int_0^\infty \rho\left(\lambda\right) E\left(\lambda\right) A_{at} R\left(\lambda\right) d\lambda \tag{2.56}$$

Here, $\rho\left(\lambda\right)$ is the spectral reflectance and $E\left(\lambda\right)$ is the spectral irradiance from external sources. We can describe the relationship between the emissivity and the reflectance

$$\rho\left(\lambda\right) = 1 - e\left(\lambda\right) \tag{2.57}$$

In the limit, and for a surface with an emissivity of 1, (2.57) shows that there is no reflectance.

Finally, the atmospheric radiance can described as

$$S_{at} = K \int_0^\infty L_{at}\left(\lambda\right) R\left(\lambda\right) d\lambda \tag{2.58}$$

where $L_{at}\left(\lambda\right)$ is the spectral radiance of the atmosphere.

Commercial imagers measure changes in the optical detector's signal levels caused by changes in the incident radiation. This signal is usually clamped to a fixed level by a signal level arising from an internal radiation source. Therefore, the detector

measures the resulting differential, given by

$$dS = S - S_0 \tag{2.59}$$

with S being the incident radiance that includes all the sources, and S_0 is the internal reference (a blackbody source $L_{\lambda,b}$) described by:

$$S_0 = K \int_0^\infty L_{\lambda,b}(T_0, \lambda) R(\lambda) \, d\lambda \tag{2.60}$$

where T_0 is the equivalent blackbody temperature of the internal source.

We can then predict what is actually recorded by the detector; this signal is then processed to separate various effects, calibrate with a well known set of parameters that ensure accuracy and repeatability. The recorded signal by the detector is

$$
\begin{aligned}
dS &= K \int_0^\infty A_{at}(\lambda) R(\lambda) \left[e(\lambda) L_{\lambda,b}(\lambda, T) + (1 - e(\lambda)) L_{\lambda,b}(\lambda, T_{sr}) \right] d\lambda \\
&+ K \int_0^\infty R(\lambda) \left[(1 - A_{at}(\lambda)) L_{\lambda,b}(\lambda, T_{at}) - L_{\lambda,b}(\lambda, T_0) \right] d\lambda
\end{aligned} \tag{2.61}
$$

This equation represents a signal that is considered an accurate representation of temperature. The drawback, however, is related to the fact that (2.61) is rather complex to be solved and displayed in real time. A compromise is needed in this case where we tradeoff accuracy for simplicity. To do so, we first consider the target to be a "gray-body" eliminating the spectral dependency of its emissivity. Secondly, we consider the transmission of the atmosphere to be independent of wavelength; this assumption is relatively realistic due to the limited spectral band of the imager. These considerations simplify (2.61) to

$$
\begin{aligned}
dS \;=\; & KA_{at}\left[e\int_0^\infty L_{\lambda,b}\left(\lambda,T\right)R\left(\lambda\right)d\lambda+\left(1-e\right)\int_0^\infty L_{\lambda,b}\left(\lambda,T_{sr}\right)R\left(\lambda\right)d\lambda\right] \\
+\; & K\left[\left(1-A_{at}\right)\int_0^\infty L_{\lambda,b}\left(\lambda,T_{at}\right)R\left(\lambda\right)d\lambda-\int_0^\infty L_{\lambda,b}\left(\lambda,T_0\right)R\left(\lambda\right)d\lambda\right] \quad (2.62)
\end{aligned}
$$

As can be seen, the above equation involves integrals that have the same form, making further simplification possible through the use of the following identity

$$
C\left(T\right)=\int_0^\infty L_{\lambda,b}\left(T,\lambda\right)R\left(\lambda\right)d\lambda \tag{2.63}
$$

Hence, (2.62) becomes

$$
dS=K\left\{A_{at}\left[eC\left(T\right)+\left(1-e\right)C\left(T_{st}\right)\right]+\left(1-A_{at}\right)C\left(T_{at}\right)-C\left(T_0\right)\right\} \tag{2.64}
$$

This differential signal is a relatively accurate and simple representation of the target's temperature referenced to an internal source. It can easily and rapidly be processed within the camera's computer to output various thermal images and temperature profiles.

This chapter focused on the development of a complete theoretical model that can be used as a baseline to validate our modeling approach and calibrate our test setup. A theoretical crack detection model requires solving the PDEs for complex geometries and in inhomogeneous media, which is only possible through the use of numerical methods.

Chapter 3

Finite Elements Formulation

3.1 Introduction

The finite elements method (FEM) is a numerical technique for approximating solutions to boundary-value problems in science and engineering. Typical mathematical physics areas where this technique is widely used include structural analysis, heat and mass transfer, fluid flow, and electromagnetics. Where the method is used as a tool for the discretization and modeling of arbitrary shaped domains and heterogeneous medium composition. It was first proposed in the 1940s in the area of structural engineering, but its use did not gain popularity until the advent of high speed computing due the fact that the resulting equations become too cumbersome to solve analytically [13].

As described in Chapter 2, the complete set of equations governing the electro-thermal system consists of two separate partial differential equations, namely Laplace's equation and the heat equation as well as the appropriate coupling conditions. The presence of defects are regarded as material inhomogeneities that render analytical solutions virtually unobtainable. Using the FEM will aid in theoretically estimating the sensitivity of the IR technique when used in the detection of hairline flaws.

In this chapter we first review and describe the basic steps of the method. Secondly, we will investigate three relevant situations: a simple three dimensional model of a cylindrical sample (where we will analyze the voltage distribution), the resulting local heating, and the major heat transfer mechanisms. A parametric two dimensional model was arranged to complete the sensitivity study where parts with surface and subsurface cracks of various sizes, shapes and orientations can be analyzed. The basic model considers at first steady state heating which we will later extend to include dynamic effects.

3.2 Finite Elements Formulation

The principle of the finite elements method is to replace a continuous domain Ω by a number of arbitrarily shaped sub-domains in which the unknown function is represented by simple interpolation functions with unknown coefficients. The following sections will discuss the basic steps in the finite elements representation. A qualitative illustration is based on solving Laplace's equation shown in (2.5) and in a 2D domain.

3.2.1 Mesh Generation

The geometry is subdivided into smaller units called elements, an operation which is called discritization or meshing. Due to its importance in the FEM, mesh generation has been the focus of extensive research, and a number of algorithms have been developed [13]. Thereby, allowing scientists and engineers to focus on the application at hand. With the increasing processing power came the ability to deploy a larger number of sub-domains as well as the accessibility to each element. Whereby, material properties are assigned at the element level.

As defined above, a mesh is a finite set of elements that can be segments (lines) in 1D,

triangles (shown in Figure 3.1) or quadrilaterals in 2D, or tetrahedras, pentahedras or hexahedras in 3D [2].
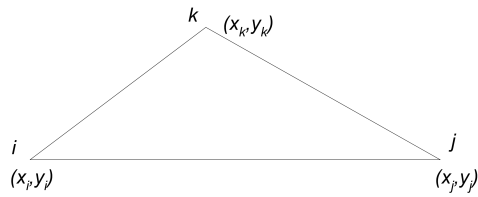
Figure 3.1: Basic triangular element and its nodal representation.

Figure 3.1 makes clear that an element is a specified by its corner points and the associated coordinates. Aim of a good mesh generation strategy is to deploy elements with equal aspect ratios with sufficiently small resolution to limit the errors to the pre-defined tolerances [17]. The nature of discritizing small defects when utilizing uniform meshing requires extensive computational resources, which may not be available if the mesh is too refined. A remedy to this shortcoming is the use of adaptive meshing, as proposed by Berger and Oliger[24]. Whereby, finer grids are adaptively placed over the coarse mesh in the sub-regions that require higher resolution.
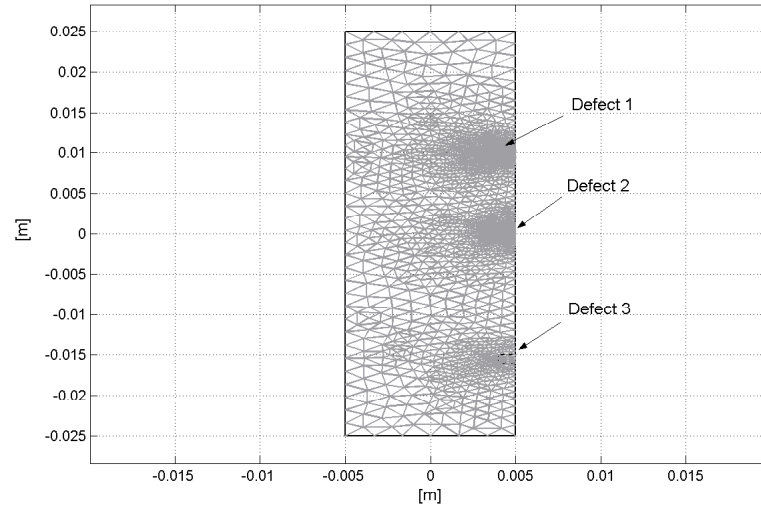
(a)
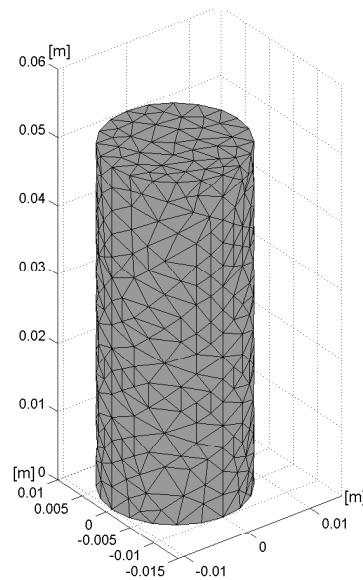
(b)

Figure 3.2: (a) Meshing of a 2D flawed part, and (b) a 3D cylindrical sample without defects.

As can be seen in Figure 3.2, the originally deployed mesh is unstructured and adaptive. For the 2D geometry with flaws the resolution had to be adjusted to capture the hairline defects. The defects seen in Figure 3.2 have the spatial characteristics illustrated in Table 3.1 .The 3D structure on the other hand was coarse as we do not

expect major changes in the field solution between adjacent elements.

Table 3.1: Defect sizes and locations.

	Length $[\mu m]$	Width $[\mu m]$	x-coordinate $[m]$	y-coordinate$[m]$
Defect 1	20	100	4.7×10^{-3}	1×10^{-2}
Defect 2	100	20	4.9×10^{-3}	0
Defect 3	500	1000	4.5×10^{-3}	-1.5×10^{-2}

3.2.2   Interpolation Function and System of Equations

The discretization of the solution domain will allow the representation of the governing equation by approximation or basis functions. The set of interpolation functions are chosen to be computationally efficient. Usually a set of polynomials of first or second order are selected.

For the 2D element shown in Figure 3.1 the approximation or interpolation function is written

$$N_i(x,y) = \alpha_i + \beta_i x + \gamma_i y \tag{3.1}$$

where α_i, β_i and γ_i are constant coefficients that can be determined using the following property of the interpolation function

$$\begin{cases} N_i = 1, \, for \, (x,y) = (x_i, y_i) \\ \quad N_i = 0, \qquad Otherwise \end{cases} \tag{3.2}$$

This will result in a local matrix equation for its constant coefficients

$$\begin{bmatrix} 1 & x_i & y_i \\ 1 & x_j & y_j \\ 1 & x_k & y_k \end{bmatrix} \begin{Bmatrix} \alpha_i \\ \beta_i \\ \gamma_i \end{Bmatrix} = \begin{Bmatrix} 1 \\ 0 \\ 0 \end{Bmatrix} \tag{3.3}$$

The solution to (3.3) shows that the coefficients depend on the area of the element (triangle in this case) and the coordinates of its nodes. Figure 3.3 depicts the interpolation function in a triangular element.
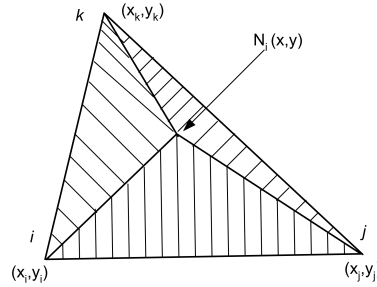
Figure 3.3: Interpolation function in the 2D FEM

We can now list the fundamental steps for solving Laplace's equation

$$\nabla^2 V = 0 \tag{3.4}$$

The basic idea is to first approximate the independent variable with a trial function

$$V \approx \hat{V} = \sum_{j=1}^{L} V_j N_j \tag{3.5}$$

Where j is the node number, L is the total number of nodes, V_j are constant coefficients for the set of equations representing the solution, and N_j are the basis functions.

The substitution of V by the trial function will result in a residual term

$$\nabla^2 \hat{V} = R \tag{3.6}$$

The best approximation for V is the one that minimizes the residual in the domain Ω. This is accomplished through forcing the residual to zero. Multiplying by a weight

function as described by the weighted residual method results in

$$\int_{\Omega} WR = 0 \tag{3.7}$$

Here W is a chosen weighting function, over the domain Ω such that

$$W = \sum_{i=1}^{L} W_i \tag{3.8}$$

Index i refers to the node number and L is again the total number of nodes in the domain.

Similarly the residual is defined as

$$R = \sum_{j=1}^{L} R_j \tag{3.9}$$

The integral in (3.7) is an inner product and suggests that W is orthogonal to R. Hence

$$\langle R, W \rangle_{\Omega} = 0 \tag{3.10}$$

Here $\langle R, W \rangle$ is the inner product between the functions R and W over the domain Ω.

Multiplying (3.6) by the weight W yields

$$\sum_{i=1}^{3} \sum_{j=1}^{3} V_j \nabla^2 N_j W_i = \sum_{i=1}^{3} \sum_{j=1}^{3} R_j W_i \tag{3.11}$$

Where 3 is the total number of nodes in the triangular element.

To force the residual to zero we integrate over the domain

$$\sum_{i=1}^{3} \sum_{j=1}^{3} V_j \langle \nabla N_j W_i \rangle_{\Omega} = 0 \tag{3.12}$$

When the domain $\mathbf{\Omega}$ is discretized into elements e (3.12) becomes

$$\sum_{e=1}^{n}\sum_{i=1}^{3}\sum_{j=1}^{3} V_j \left\langle \nabla N_j W_i \right\rangle_e = 0 \tag{3.13}$$

Where n is the total number of elements deployed in the solution domain $\mathbf{\Omega}$.

To apply the boundary conditions we integrate by parts

$$\sum_{e=1}^{n}\sum_{i=1}^{3}\sum_{j=1}^{3} \left[-\left\langle \nabla N_j \cdot \nabla W_i \right\rangle_e \right] \{V_j\} = \left\{ -\oint_e \left(\nabla N_j \cdot \mathbf{n} \right) W \, dS_e \right\} \tag{3.14}$$

Where S_e is the area of the sub-domain e.

We can easily construct the system of equations from (3.14) where the local matrix elements are

$$a_{ij} = -\left\langle \nabla N_j \cdot \nabla W_i \right\rangle_e \tag{3.15}$$

This expression underlines the importance of selecting a computationally efficient weighing function. A number of formulations have been developed based on specific choices for this function, most notably Galerkin's. Here W_i is chosen to be equal to the trial function

$$W_i = N_i \tag{3.16}$$

The final step involves solving the system of equations while including the boundary conditions. The general expression is

$$[A] \{V_j\} = \left\{ -\oint_e \left(\nabla N_j \cdot \mathbf{n} \right) W \, dS_e \right\}$$

3.3 3D FEM Modeling

This introductory model will focus on the solution for both Laplace's equation and the steady state heat equation while, at the same time considering coupling conditions and the appropriate boundary conditions. Using FEMLAB we solve for the electric potential, then use this solution to determine the heat source and subsequently find the temperature distribution.

3.3.1 Voltage Distribution

An electrostatic model of a 3D cylinder was created with uniform conductivity. We define the following parameters:

- Length of cylinder: $L = 0.05\,m$.

- Radius of cylinder: $R = 0.01\,m$.

- Electrical conductivity: $\sigma = 5 \times 10^4\,S/m$.

For the boundary conditions, we specify the inward normal component of the current density as in (2.20) with

$$\mathbf{n} \cdot (\sigma \bigtriangledown V) = -\mathbf{n} \cdot \mathbf{J} = 32000 A/m^2 \tag{3.17}$$

This is equivalent to a total input current of 10A. For the remaining boundaries, we adopt the conditions specified in (2.21).

With the parameters specified above, we predict the voltage drop from the top of the part to the bottom to be:

$$V = I\frac{L}{\sigma A} = \frac{L}{\sigma}J = 0.482V \tag{3.18}$$

where A is the cross-sectional area of the cylinder.

The solution is presented in Figure 3.4 as a slice view displaying the voltage distribution throughout the volume of the part.
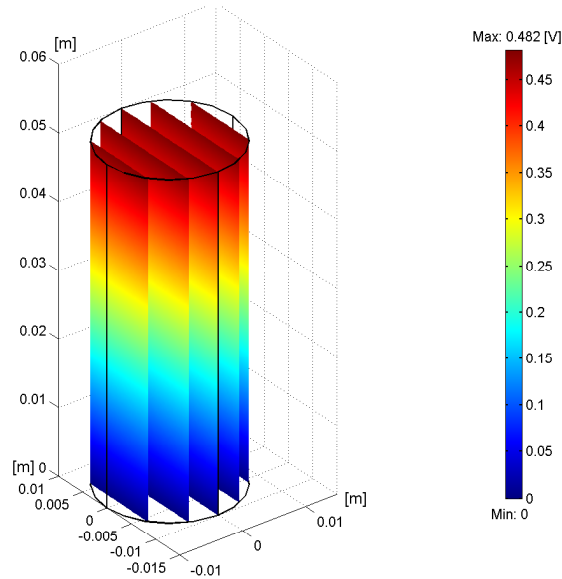
Figure 3.4: Voltage distribution for a cylindrical compact of constant conductivity driven by a current of 10A.

The electric potential V results in a heating power Q proportional to its magnitude as illustrated in (2.30), where the constant of proportionality is the conductivity σ.
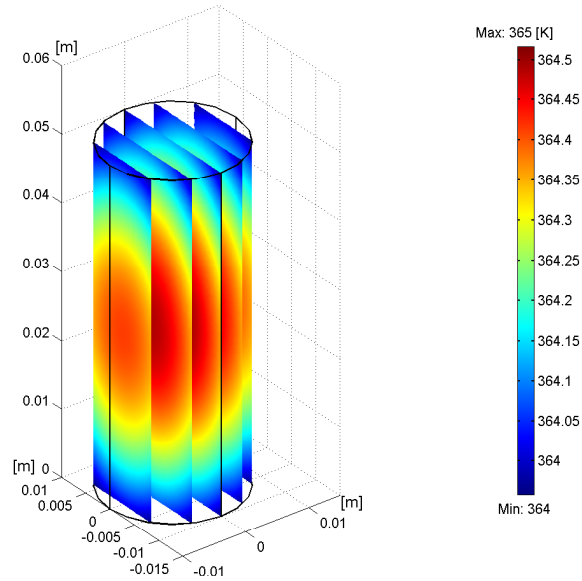
3.3.2 Temperature Distribution

The thermoelectric heating model includes the voltage solution obtained from the electrostatic model used to compute the heat sources. The source is the deposited power and the dominant heat transfer mechanism is conduction while the boundaries are convective. It is assumed that the part is cooled through natural convection.

In addition to the dimensional parameters listed above, we define the thermo-physical properties of the part as follow :

- Material Density : $\rho = 7250 \, kg/m^3$.

- Heat capacity: $c = 440 \, W/kg \, °C$.

- Thermal conductivity: $k = 40 \, W/m \, °C$.

- Convection heat transfer coefficient: $h = 10 \, W/m^2 \, °C$.

The boundary conditions as in (2.46) and (2.47) are set to be of flux or Neumann type. These conditions will result in a temperature distribution presented in Figure 3.5. Also shown in Figure 3.5 is a line profile along the z-axis.

(a)
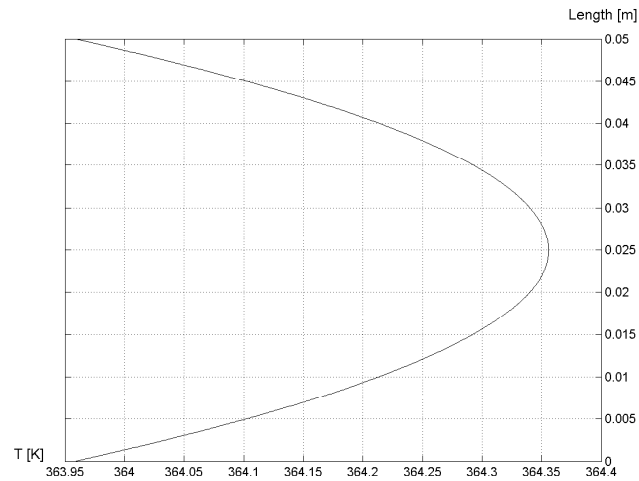
(b)

Figure 3.5: (a) Temperature distribution in an unflawed cylindrical compact, and (b) surface temperature profile along the z-axis in Kelvin.

Similar to the temperature distribution obtained through the analytic solution, the temperature is at its maximum at $z = r = 0$ and decays until it reaches a minimum at the surface.

3.4 Sensitivity Study

To validate the applicability of the IR imaging technique for the detection of surface cracks and subsurface defects, it is necessary to first evaluate the temperature changes and ensure that they fall within the detection limits of our imager with reasonable margins. The theoretical defect sizes we are considering are on the order of $20\mu m$, which can be computationally cumbersome. However, a 2D representation of surface and near-surface defects appears sufficiently adequate to investigate the sensitivity of our method.

This analysis is subdivided into two sections, the first focuses on the steady state condition, i.e., no time component is included. Second, we extend the previous model to include transient effects and consequently estimate the response time of the technique.

The defects we consider are voids with spatial parameters listed in Table 3.1 and the following thermo-physical properties:

- Material Density : $\rho = 1.18\,kg/m^3$.

- Electrical conductivity: $\sigma = 35 \times 10^{-15}\,S/m$.

- Heat capacity: $c = 1005.7\,W/kg\,°C$.

- Thermal conductivity: $k = 0.026 W/m\,°C$.

3.4.1 Steady-State Model

The steady state model allows us to confirm the shortcomings of a thermographic system based on imaging a part at equilibrium when actively heated (through an external source). The following figure depicts the current density in the part.
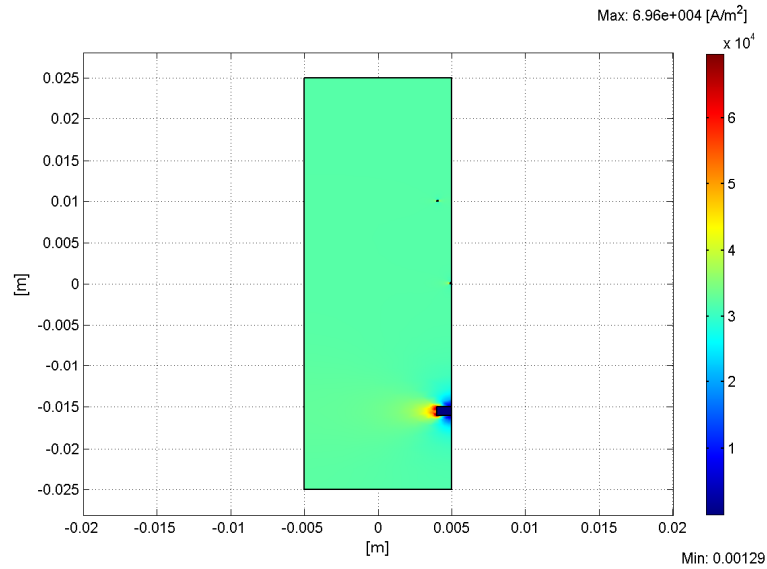
Figure 3.6: Current density distribution in a flawed sample.

Here we notice a current crowding effect that takes place in the space immediately surrounding the defect. Clearly, crowding causes higher temperature gradients in these specific areas.

The current deposits power and hence causes the temperature of the part to rise to an equilibrium temperature. This temperature distribution and the subsequent surface temperature profile are shown in Figure 3.7.
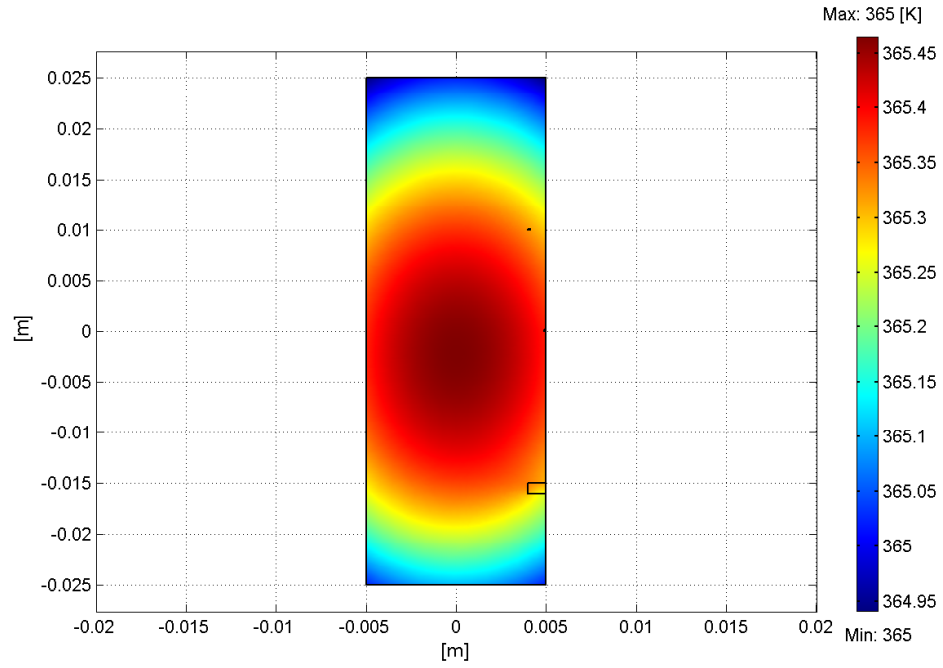
(a)
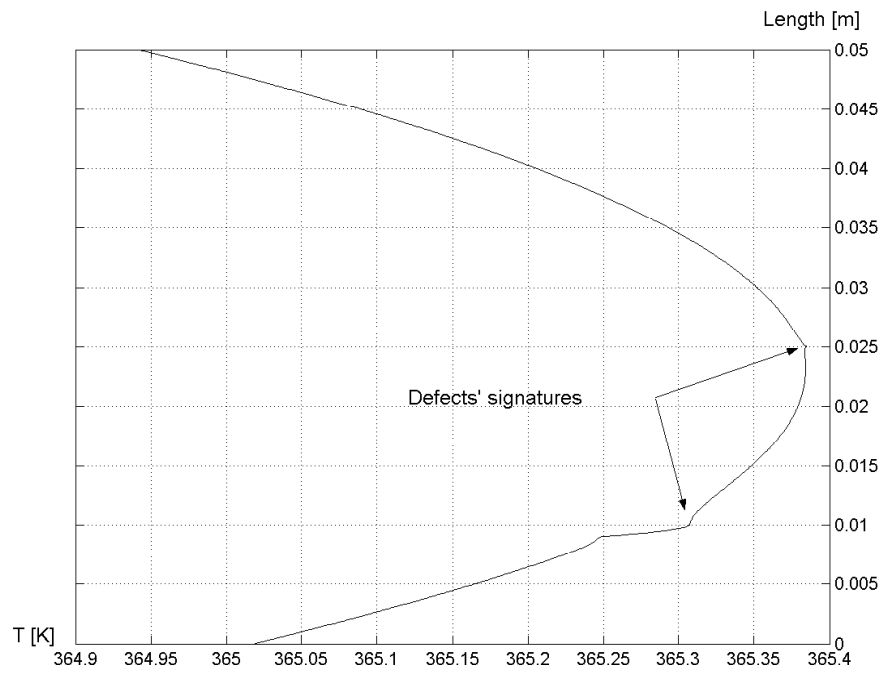
(b)

Figure 3.7: (a) Steady-state temperature distribution in a flawed compact, and (b) the surface profile along the z-axis.

As can be seen, surface cracks are clearly visible. However, the resulting temperature signatures varies with flaw size and orientation. Smaller defects, although they produce a gradient, are too small to be detected. Moreover, subsurface defects do not produce a noticeable signature. However, we proceed to a dynamic testing situation by analyzing the part when it is subjected to a step current.

3.4.2 Time-Dependent Thermal Model

Voids or inclusions posses thermo-physical properties that are very different from those of the actual material. Consequently, the heating rate will be different. Furthermore, a transient excitation will cause a diffusion process to take place in the part, wherein a thermal gradient appears on its surface. Dynamic thermography, where a thermal image is taken in real time, offers the possibility to capture this time dependent process and subsequently allowing the detection of subsurface defects and small surface breaks.

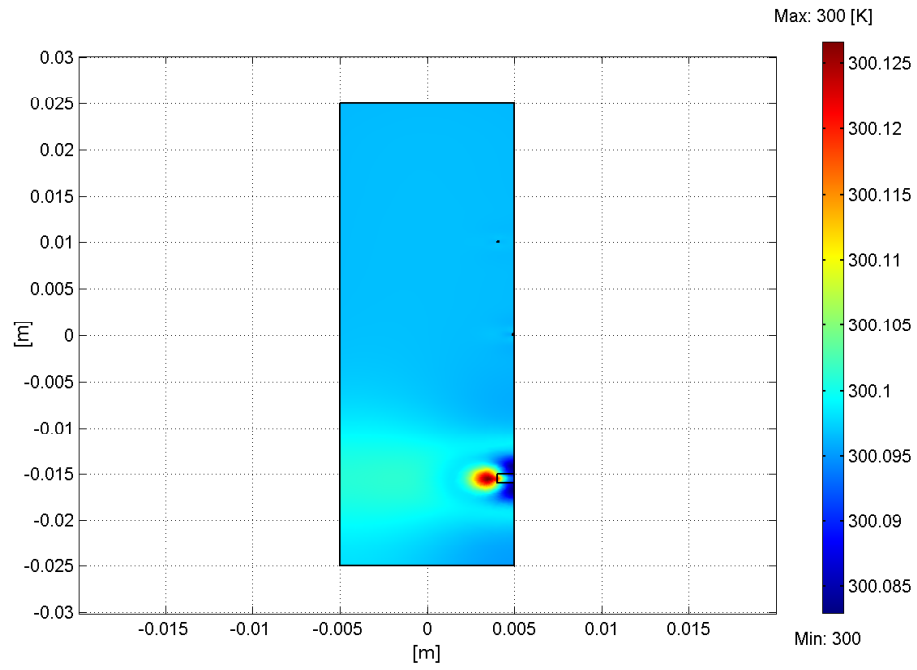The following set of figures shows the transient thermal response to a step current excitation.
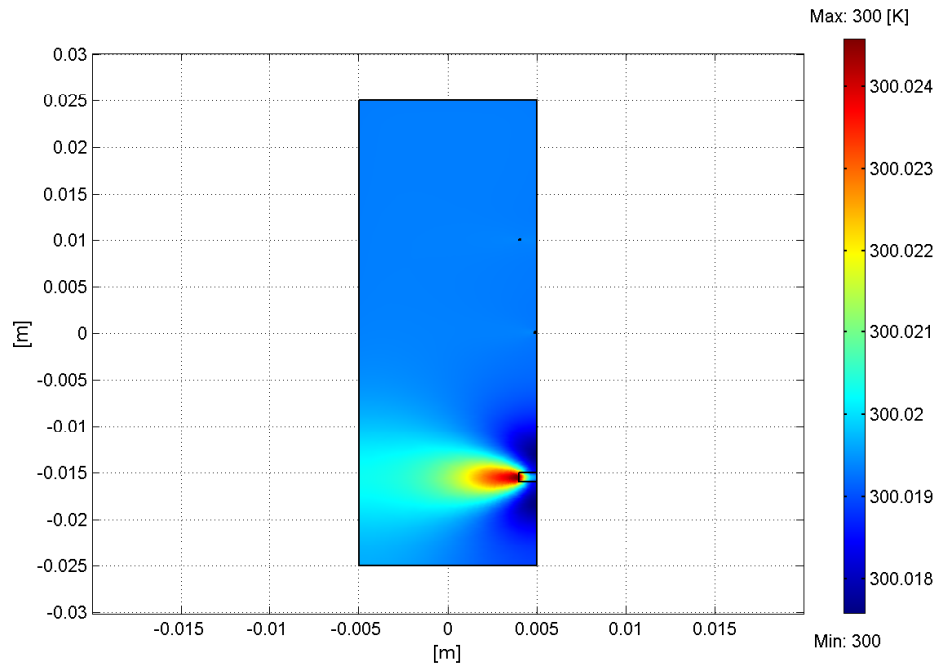
(a)
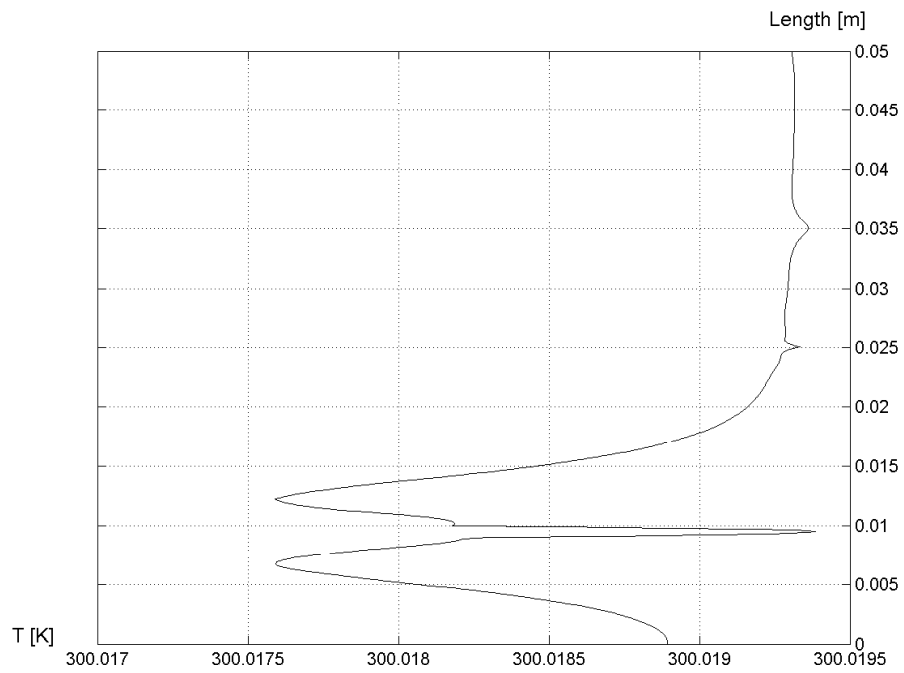
(b)

Figure 3.8: (a) Surface temperature after 0.2 sec, and (b) profile along the z-axis.

(a)

(b)

Figure 3.9: (a) Surface temperature after 1 sec, and (b) profile along the z-axis.

(a)
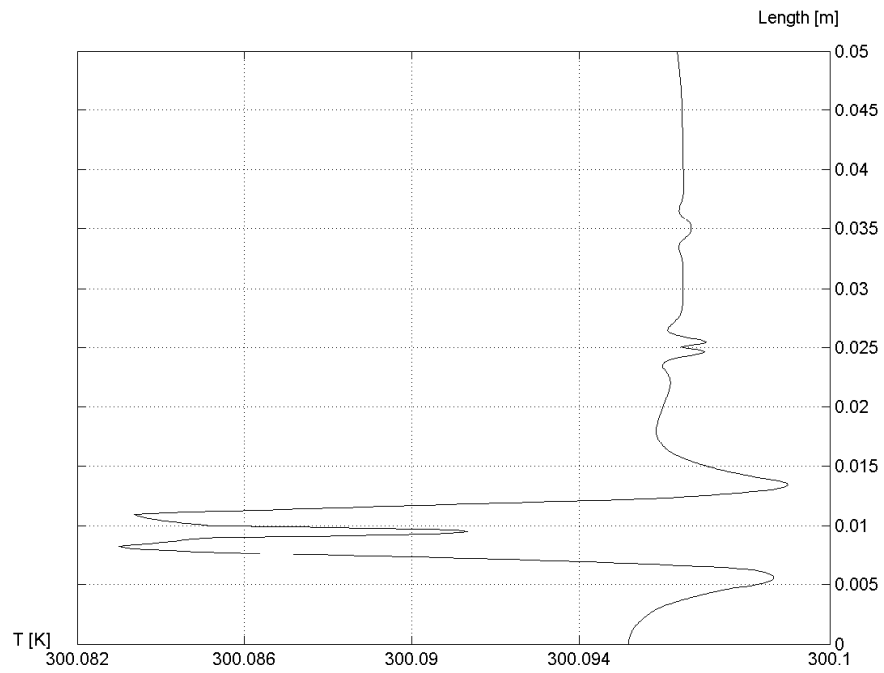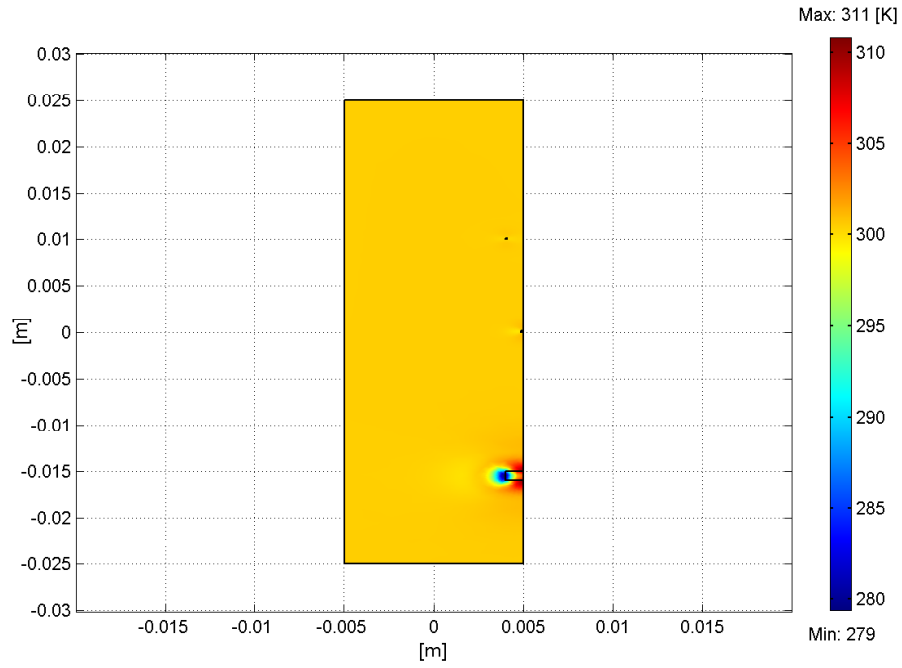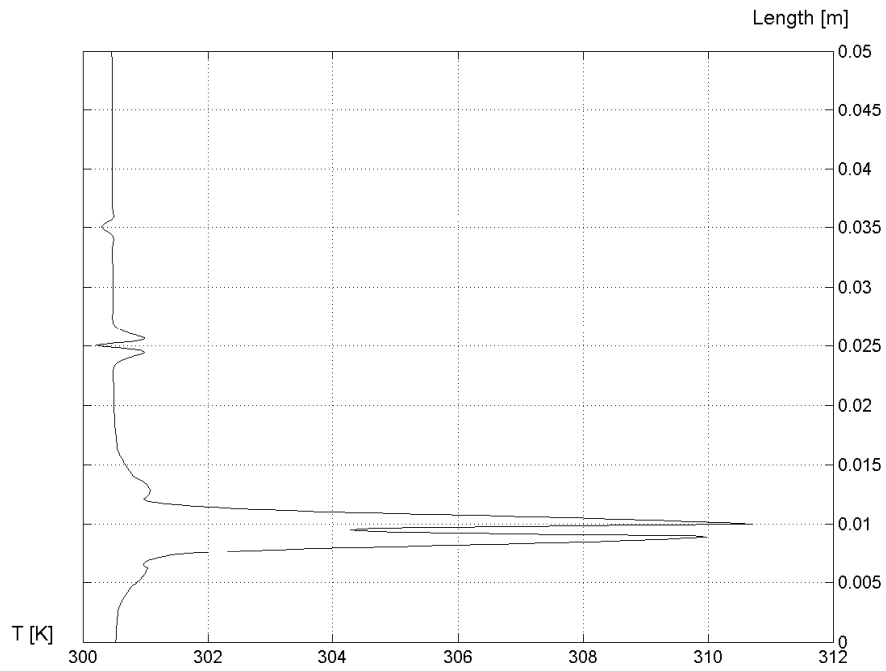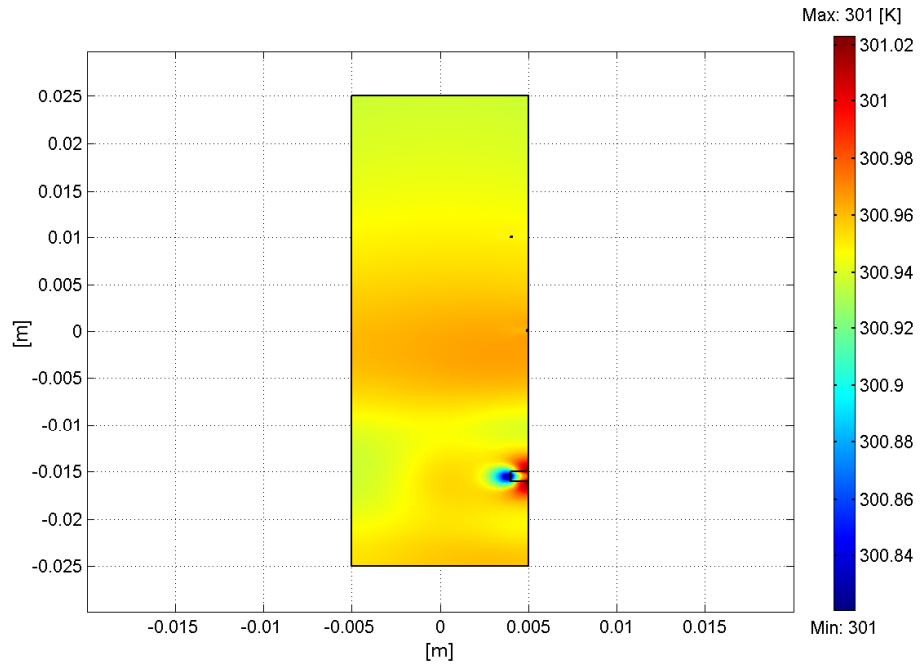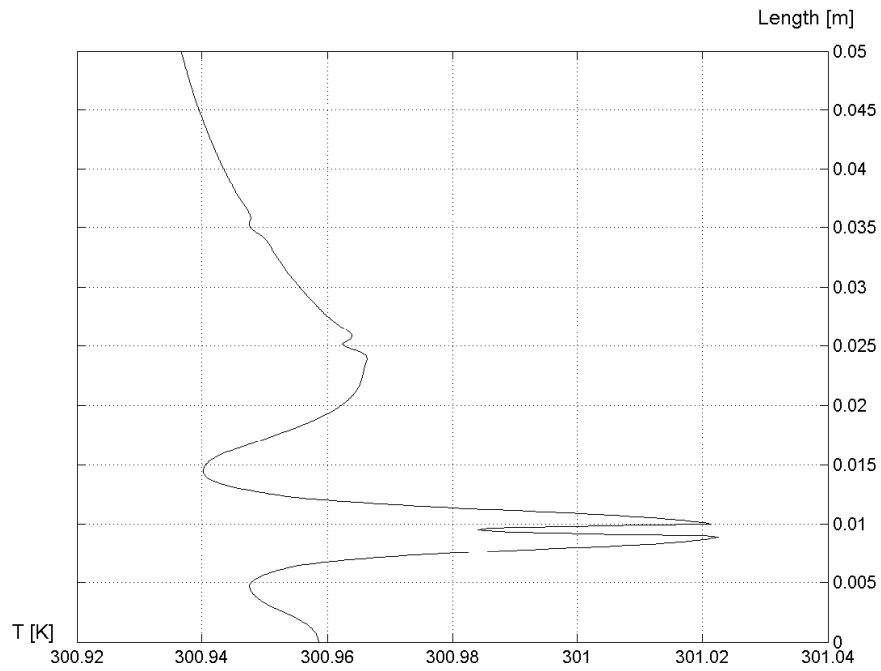

(b)

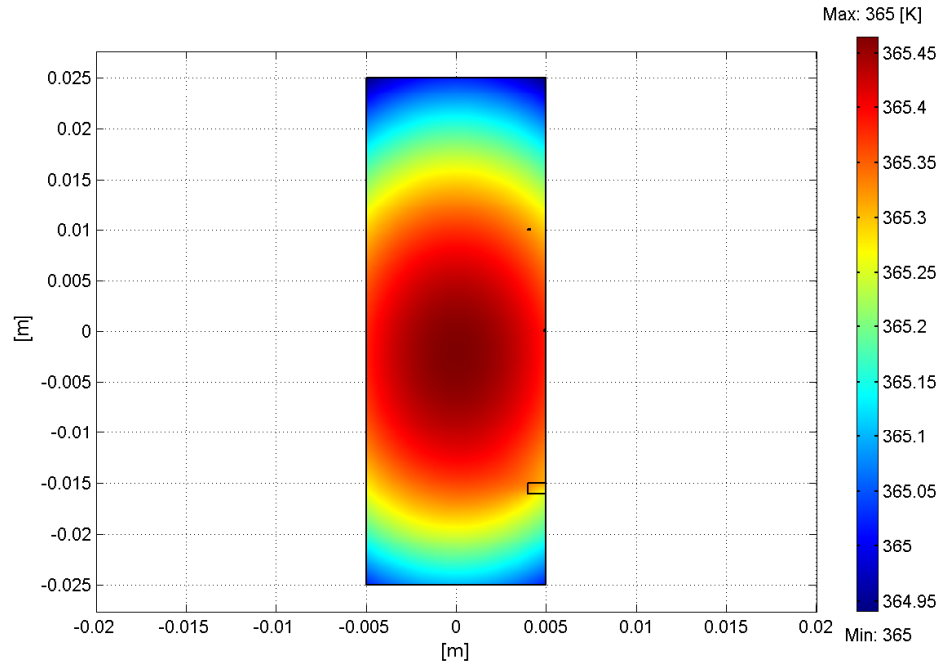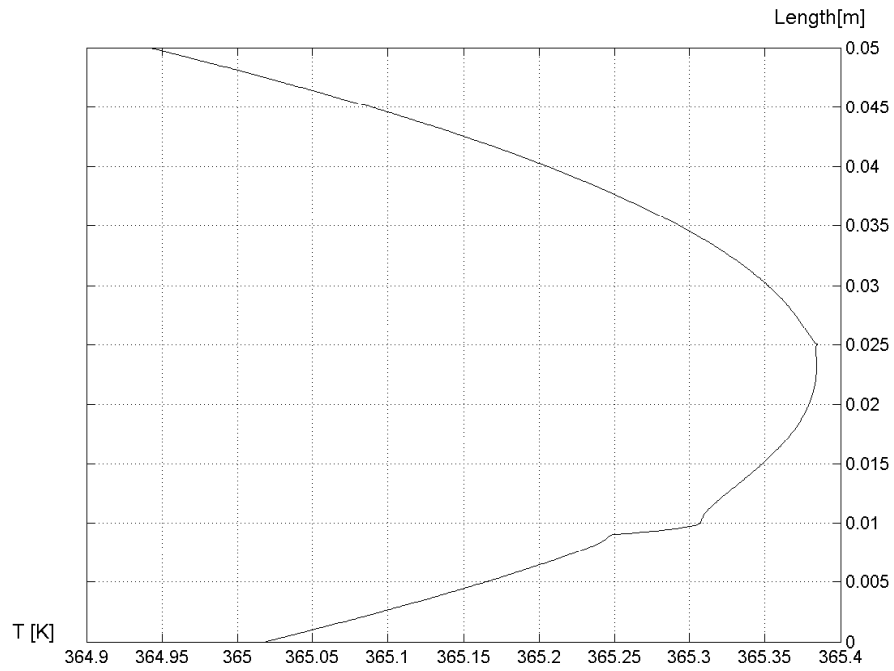**Figure 3.10:** (a) Surface temperature after 5 sec, and (b) profile along the z-axis.

(a)

(b)

Figure 3.11: (a) Surface temperature after 10 sec, and (b) profile along the z-axis.

(a)

(b)

Figure 3.12: (a) Surface temperature at equilibrium, and (b) profile along the z-axis.

From these figures we conclude that dynamic thermography offers significant advantages, including the possibility to detect subsurface defects and very small surface-breaking flaws. The results summarized in Figure 3.13 show a distinguishable signature from a small surface crack. A noticeable temperature change definitively indicate the presence of a subsurface defect.
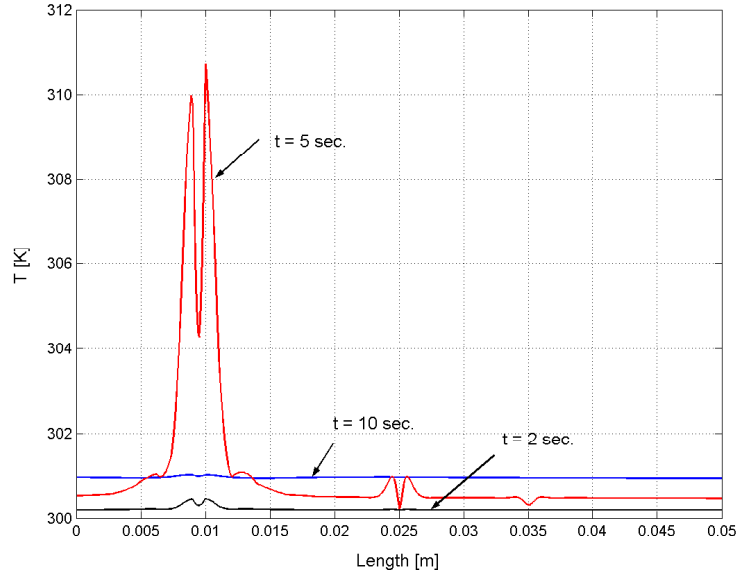
Figure 3.13: Temperature profile along the z-axis at various time steps increments.

The data plotted in Figure 3.13, reveal the detection limits for the simulated flaws. This also sets the performance requirements of the IR imager and allows the establishment of test conditions. Table 3.2 lists the preliminary requirements.

Table 3.2: IR camera requirements

Requirement	min.	commercial camera
Frequency	$2\,Hz$	$30\,Hz$
Thermal sensitivity	$0.2\,°C$	$0.08\,°C$
Spectral range	$8 \sim 10\,\mu m$	$7 \sim 13.5\,\mu m$

After estimating the sensitivity of the method and establishing the equipment requirements, we then proceed to the experimental measurements. The camera, whose parameters are listed in Table 3.2, provides sufficiently large margins for realistic measurements that include environmental effects and all possible uncertainties.

Chapter 4

Experimental Study

4.1 Introduction

Our experimental study focuses first on capturing static and dynamic thermal images of green-state compacts subject to DC current excitation. This step will enable us to establish a measurement baseline that includes radiation effects from the surroundings. Second, the static and dynamic IR imaging is next deployed for the detection of surface defects within green-state parts. However a complete detection system requires two additional components: a display component whereby the captured thermal image is displayed in a comprehensive manner and an image processing and evaluation component is related to assessing the integrity of the sample from the constructed image. Here, basic image analysis techniques such as profiling and thresholding are employed.

All these techniques and requirements are combined to constitute a complete detection system. The next sections will first introduce the test arrangement then present a set of results from static and dynamic testing. For this purpose a set of P/M samples were used with different powder and lubricant constitutions as well as a variety of characteristics such as density and shape.

4.2   Test Arrangement

We have configured a simple IR imaging arrangement (see. Figure 4.1) which includes
at its core an IR camera with performance specifications listed in Table 3.2.   In
addition to the camera, equipment is configured such as a DC power supply, a data
collection and analysis computer, and electric contacts to allow the injection of DC
current.
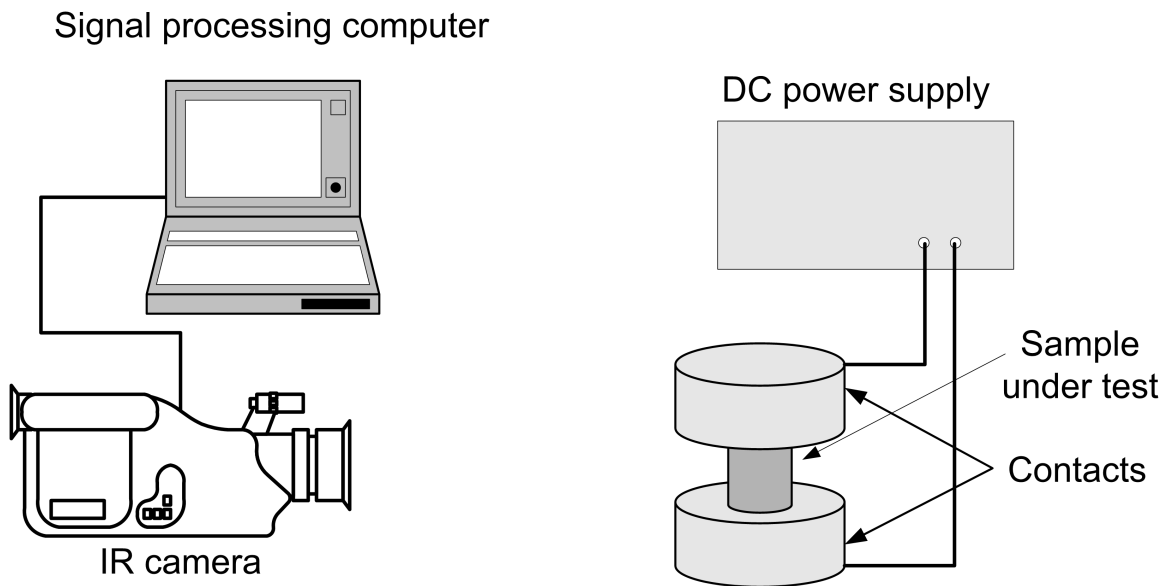
Figure 4.1: Experimental test arrangement.

The current injection scheme utilizes a setup with two large aluminum block contacts
to maintain uniform current flow into the part. The contact pressure of the electrodes
is set by a stepper motor in order to maintain a constant pressure on the part, and
to keep the contact resistance low.

Figure 4.2: Generic test arrangement showing the electrode contacts.

Figure 4.2 details the test arrangement where the camera is located at a distance of approximatlyapproximately $0.3m$ away from the area of interest. Figure 4.3 depicts the stepper motor driven press system that applies constant pressure on the aluminum blocks that serve as electric contacts for the sample under test.
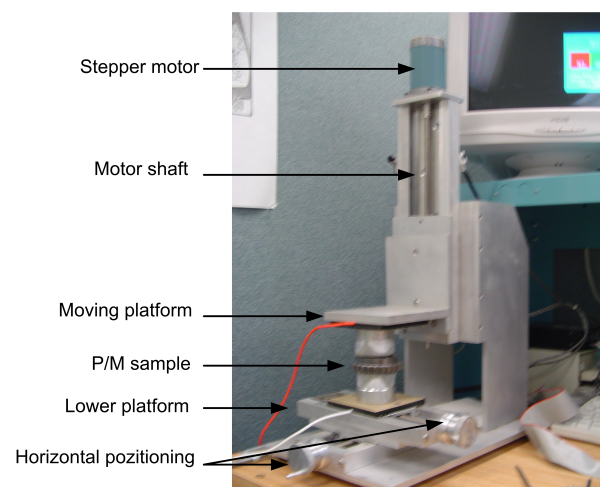
Figure 4.3: Press system with operational details.

4.3 Static IR Detection and Image Processing

In an effort to evaluate the effects of flaw size, shape, and orientation, a number of defects were artificially created. In particular, using a simple exacto knife we have created surface defects whose dimensions are listed in Table 4.1 .

**Table 4.1:** Flaw parameters in a green-state cylindrical part.

Flaw #	Length [*mm*]	Width[*μm*]	Depth [*μm*]	Orientation [*μm*]	Location [*cm*]
1	10	< 20	< 20	Horizontal	1
2	1	20	20	Horizontal	2
3	2	20	20	Vertical	3
4	10	< 20	< 20	Vertical	5

These defects were created in a cylindrical part consisting of 1000B powder without lubrication. This part was subjected to a DC current flow of 20A. The next step involves the IR image acquisition, storage in a PC, and Matlab post-processing by setting a threshold. Figure 4.4 illustrates the IR image taken from the part described in this section prior to any processing. The image obtained is an index image format which is transformed in the camera to a gray-scale. It takes the form of an intensity matrix where the intensity of each pixel is in the range from 0 , to 255. The elements in the intensity matrix represent gray levels with 255 representing full intensity [5]. This image is later paletted for viewing using a simple coloring scheme (using Matlab) where the base temperature is encoded in green, cooler areas are represented in blue and hot spots are in red.
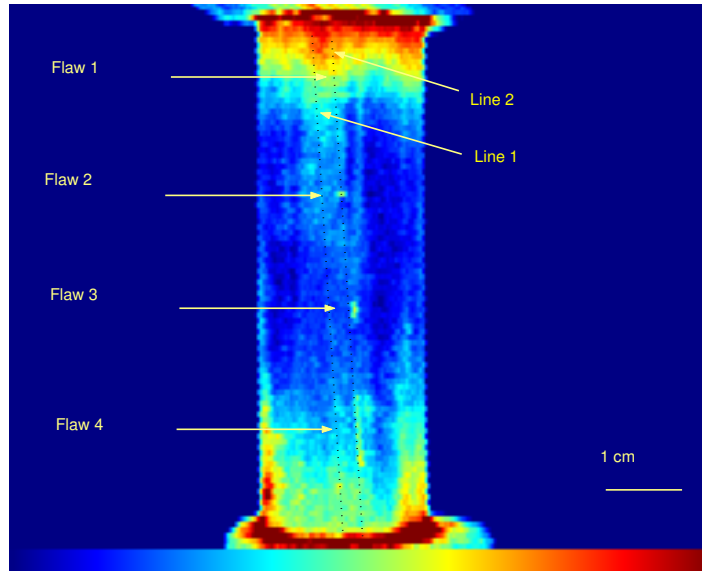
Figure 4.4: Generic IR image recording from a cylindrical part.

To quantify the temperature gradient caused by the presence of a defect we generate a line profile along the part, precisely intersecting the area of interest. Figure 4.5 depicts the image profile along a line that traverses across all defects and a second line parallel to it crosses a flawless area.
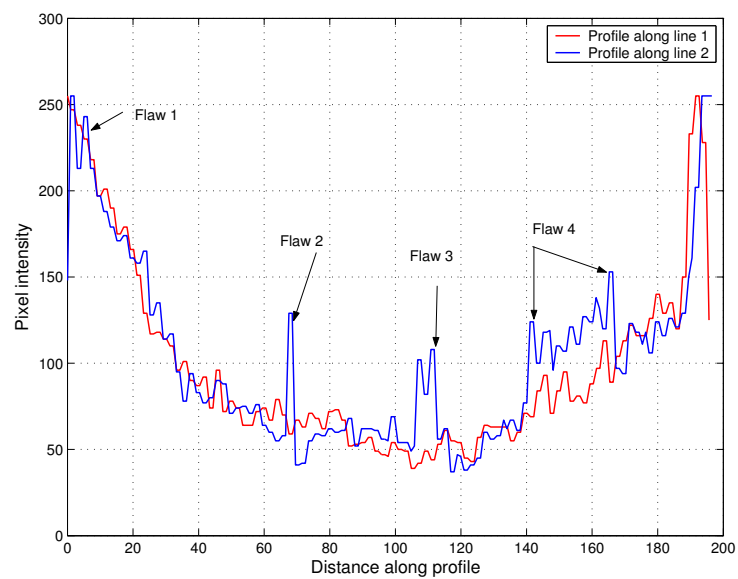
Figure 4.5: Profile along the two dotted lines in Figure 4.4 , with a spatial pixel to pixel distance of 300*μm*.

In a post-processing step, we separate the thermal gradients due to defects from the effects of material density variations, contact resistance and reflections. A differential plot, where intensity values along line 1 are subtracted from values along line 2 results in the profile shown in Figure 4.6.
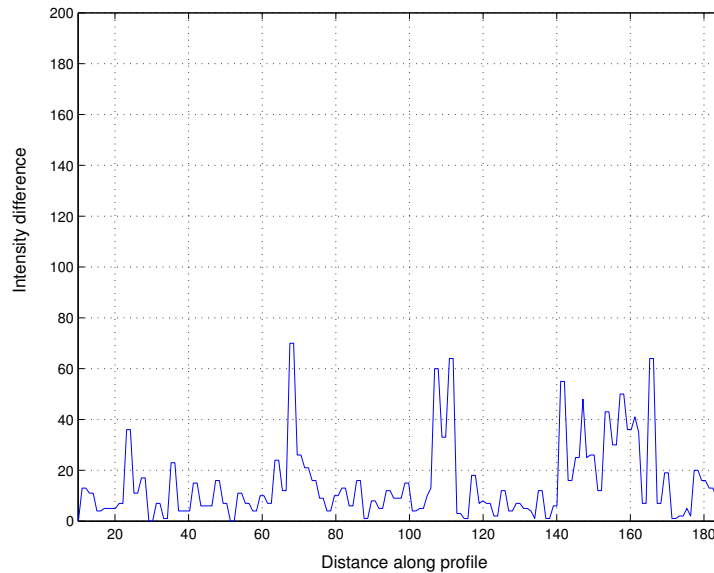
Figure 4.6: Difference in intensity between the pixels along line 1 and line 2 shown in Figure 4.4.

Applying simple image processing techniques, it is shown that qualitative flaw information can be gained. The thresholding concept is based on the idea of selectively eliminating areas with temperatures below a preset value. Many algorithms have been proposed to automate this operation. A simple scheme utilizes the histogram (the representation of the number of pixels at each level), while the more elaborate algorithms use contextual and statistical information including information from adjacent pixels [5].

A Matlab program was written to set an intensity threshold and convert the image into a "binary" representation. In other words, a two level representation where all pixels whose values reach or exceed the threshold value are assigned to a "bright" category. Pixels with values below the preset value are assigned to a "dark" category.

Figure 4.7 represents the previous IR image after thresholding.
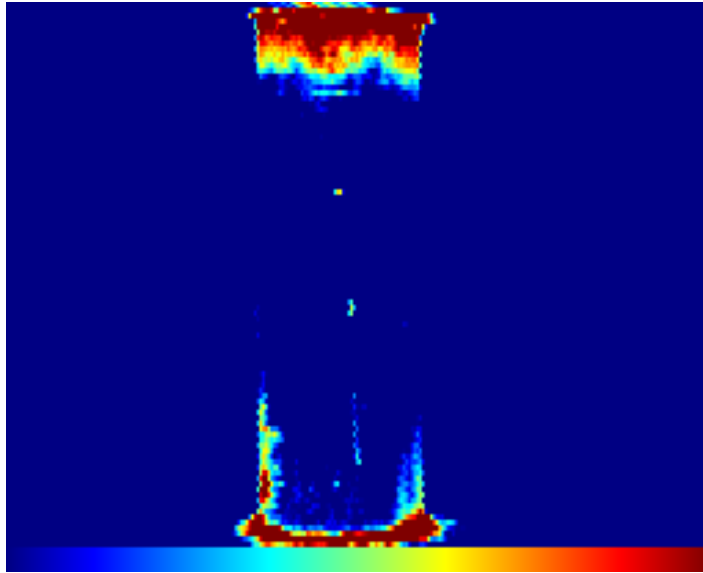
Figure 4.7: IR image of Figure 4.4 part after thresholding.

Here, the defects' signatures are more visible making a go, no-go type of evaluation possible.
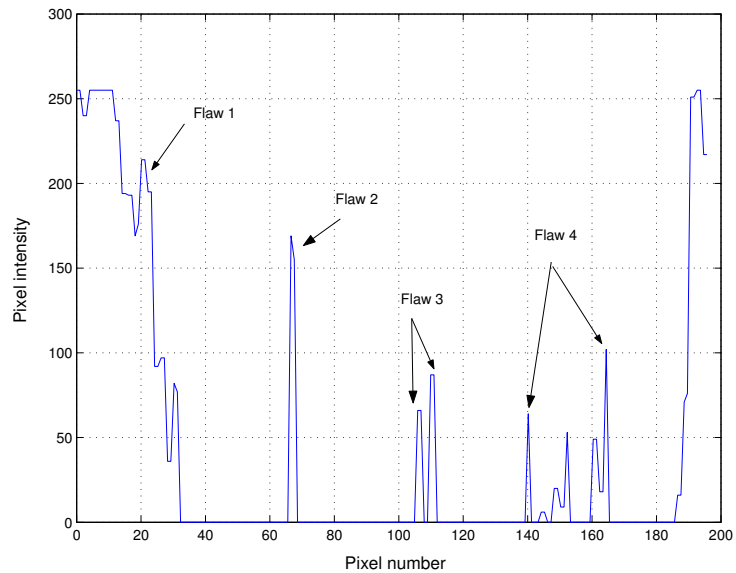
Figure 4.8: Temperature profile along the center line of the image after thresholding with a spatial pixel to pixel distance of $300\mu m$.

The results presented in this section show that sizeable flaws can easily be detected through a steady state test arrangement. However, as was demonstrated in the theoretical modeling, very small surface cracks and subsurface defects cannot be detected; they require a dynamic test arrangement.

4.4   Dynamic Testing of Simple and Complex Compacts

This section discusses dynamic testing whereby P/M samples are subjected to a current step function. A solid state switch is used in conjunction with a DC power supply to generate a well shaped current step.

We tested a number of simple green-state parts with different material and lubrication constituents and varied densities. We also tested complex and multilevel parts with surface defects. The complex samples include surface breaks located between levels and in other areas that constitute a challenge for the part manufacturers.

4.4.1   Simple Green-State and Sintered Compacts

The parts tested here were provided by Nichols Portland [32]. These parts are rectangular in shape with dimensions of $3.175\,cm \times 1.27\,cm \times 1.27\,cm$. The material used in making the samples is FC-0205, which is a mixture of Iron, 2% Copper and 0.5% Carbon. The same number of parts was tested with 0.55% EBS lubricant or die wall lubrication (DWL). For the purpose of observing the influence of density on the heating, the tested samples were compacted to various densities: $6.6\,g/cm^3$, $6.9\,g/cm^3$, and $7.2\,g/cm^3$. The test also included finished parts where we tested a similar set of compacts after sintering.

The following outlines an IR recording sequence of green-state part with a density of $6.9\,g/cm^3$ and 0.55% EBS lubricant.

(a)

(b)
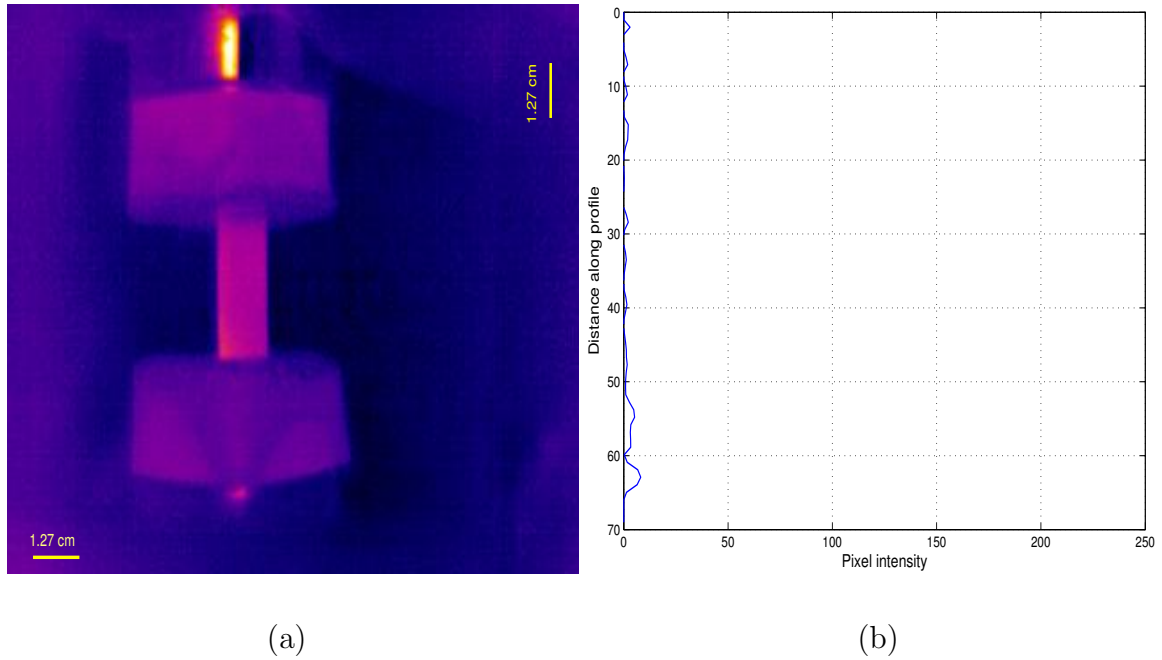
Figure 4.9: (a) IR recording at $t = 0\,sec.$, and (b) profile along the center line with a spatial pixel to pixel distance of $500\mu m$.

(a) (b)
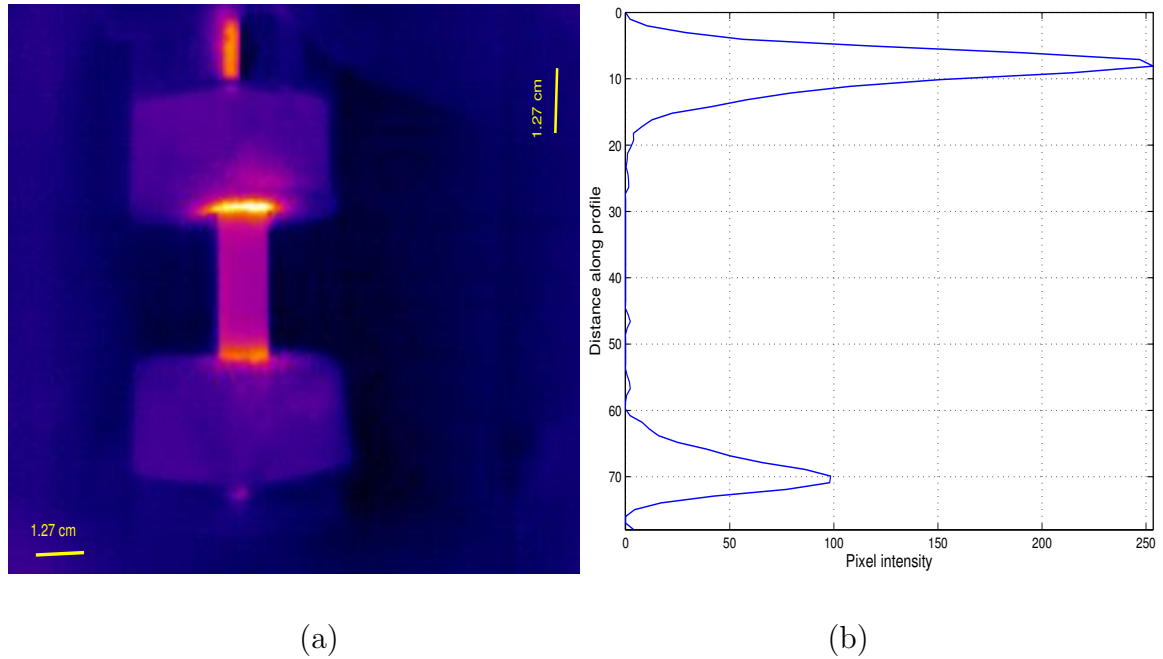
Figure 4.10: (a) IR recording at $t = 2\,sec.$, and (b) profile along the center line with a spatial pixel to pixel distance of $500\mu m$.

(a) (b)
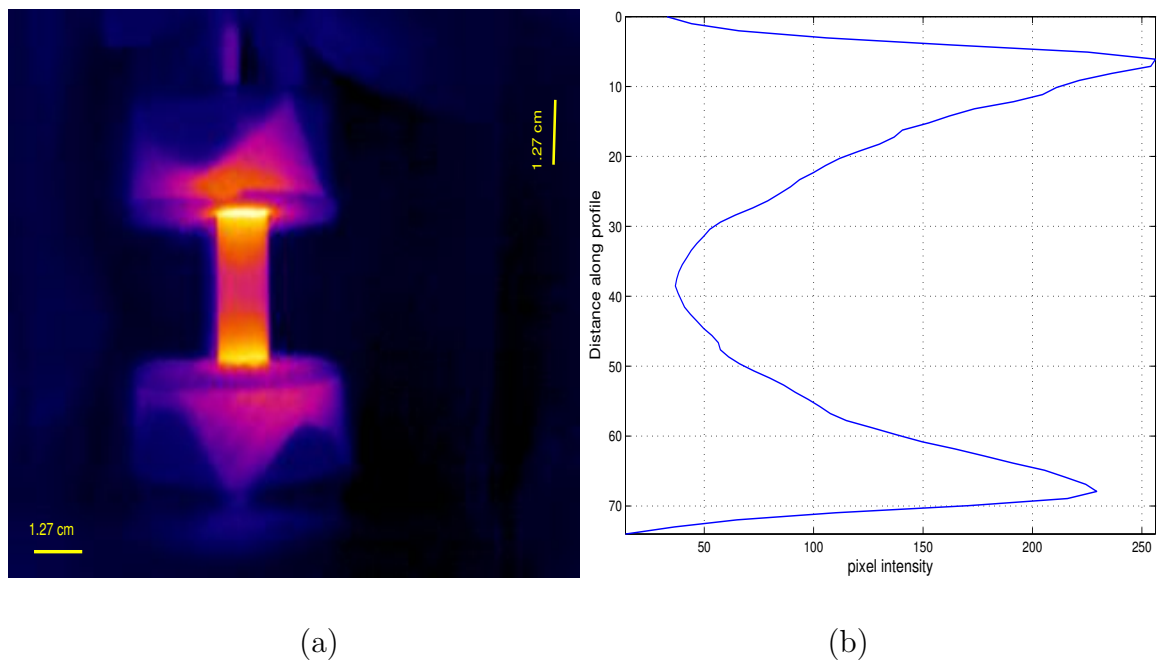
Figure 4.11: (a) IR recording at $t = 15\,sec.$, and (b) profile along the center line with a spatial pixel to pixel distance of $500\mu m$.

(a)   (b)
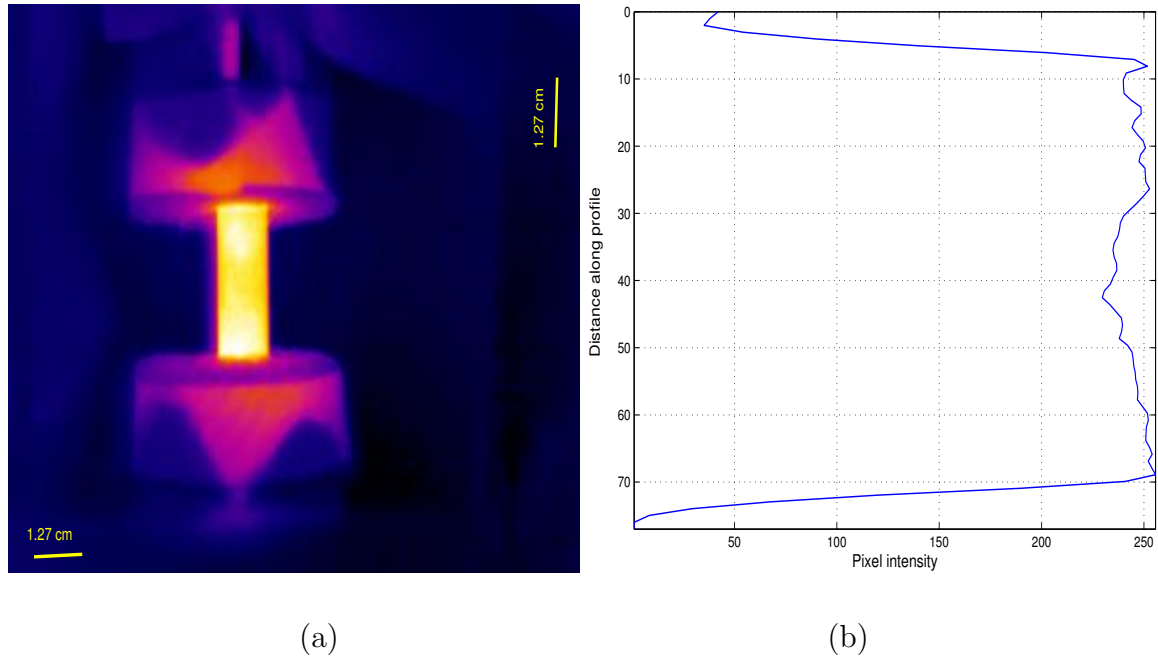
Figure 4.12: (a) IR recording at $t = 25\,sec.$, and (b) profile along the center line with a spatial pixel to pixel distance of $500\mu m$.

The dynamic behavior captured for all the parts tested is very similar, with the only differences being the rate of temperature rise and the final steady-state temperature level. Similarly, sintered parts were tested and the behavior followed the same trend. However the temperatures attained when the same current step is applied are much lower (approximately $10\,^{\circ}C$) due to the high electric conductivity and consequently the low power deposition.

In addition to testing parts with different densities, we have conducted a preliminary statistical study to determine the repeatability of the testing. A small number of green-state samples with similar construction (material composition, density and lubricant) have been tested in an effort to establish a baseline. Figure 4.13 illustrates the intensity profiles from the three parts with the end blocks included to observe the effects of the contact resistance. These images were taken 10 seconds after applying the current pulse.
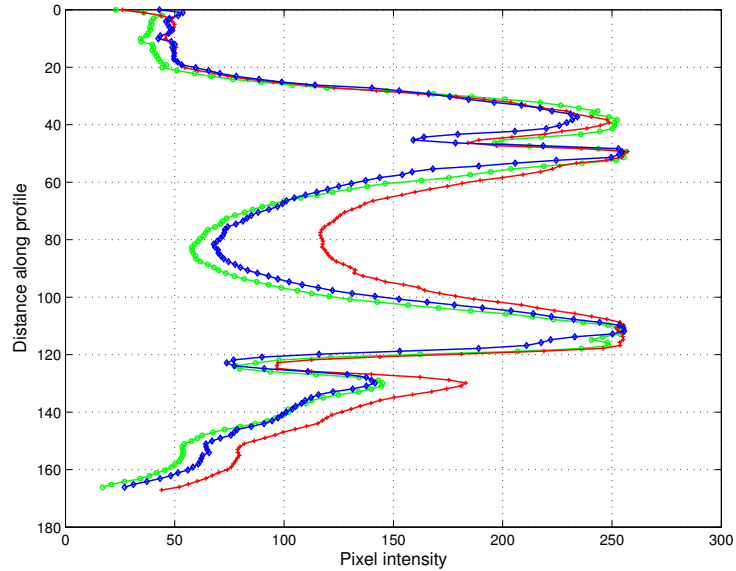
Figure 4.13: Repeatability plot, showing profile along the center line from three green-state samples, with a spatial pixel to pixel distance of $500\mu m$.

We note that the three profiles are very similar in shape, but show small differences in the absolute intensity. The differences are due to the uncontrolled test conditions including a fixed temperature range, the loose control of the time variable, and environmental conditions.

4.4.2 Complex Green-State Compacts

In an effort to test the method with complex parts, compacts were procured from Plansee AG [33]. As shown in Figure 4.14, the parts are two-level gears and where the first level includes a ring of teeth. The first level has the dimensions of $9\,mm$ (height) by $75\,mm$ (outer diameter). The dimensions for the second level are $11\,mm$ (height) and $59\,mm$ (outer diameter).

Figure 4.14: Green-state multilevel samples [33].

Figure 4.15 depicts the locations and nature of the surface cracks in these complex parts. Here the cracks are typically less than **20μm** in size.

(a) (b)
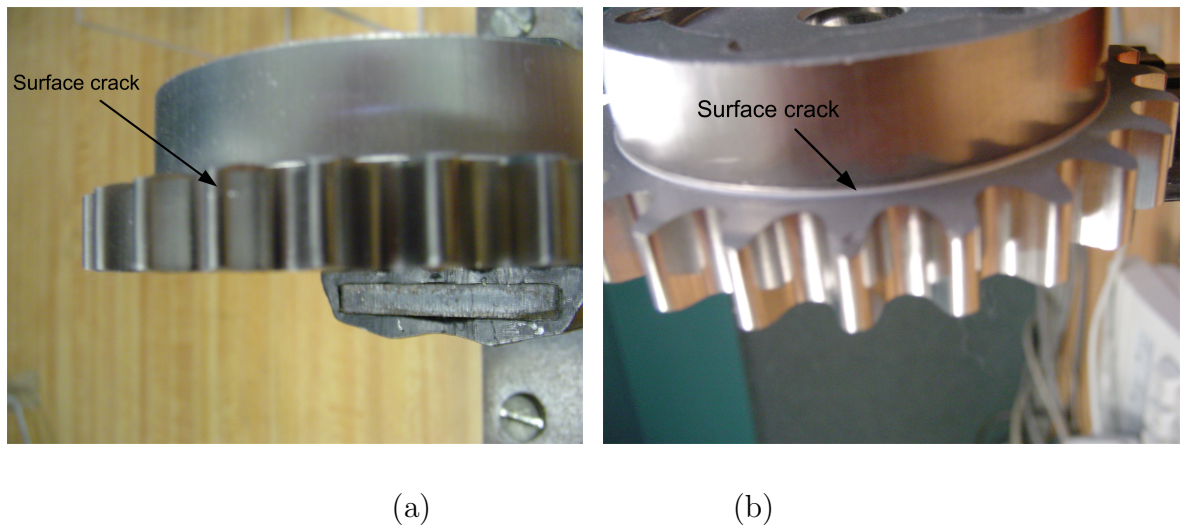
Figure 4.15: (a) Surface crack on the gear-tooth, and (b) a surface crack located at the level transition in a complex gear.

As can be noticed, the parts shown are very shiny, with an emissivity on the order of 0.2. This makes an IR measurement a challenge due to undesired reflections. The

emissivity was determined by measuring the temperature of a reference point on the surface of the part using a thermocouple. Adjusting the emissivity setting (used by the IR instrument for corrections) allowed us an adjustment until the camera's temperature reading matches that of the thermocouple.

Two types of IR tests were performed. First, a similar scheme as for simple parts was implemented. DC current was injected into the sample through surface contacts. Second, the current was directed towards the area of interest, while the IR camera points to the same area.

The camera was located $0.3m$ away from the sample, and the temperature range was set to be automatically adjusted to accomplish better sensitivity. The automatic range takes the lowest temperature and the highest as detection limits. The lowest setting is the background, which is at room temperature, i.e. at $27°C$.
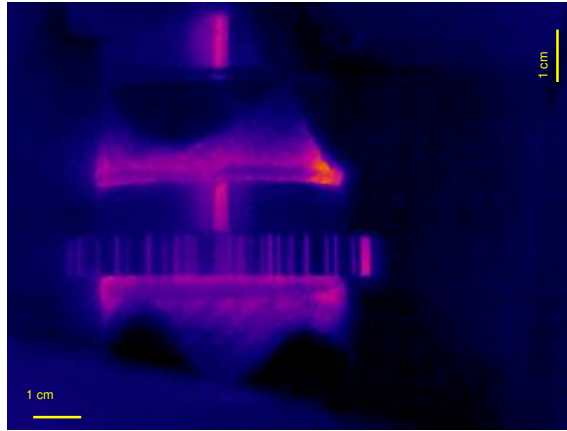
(a)
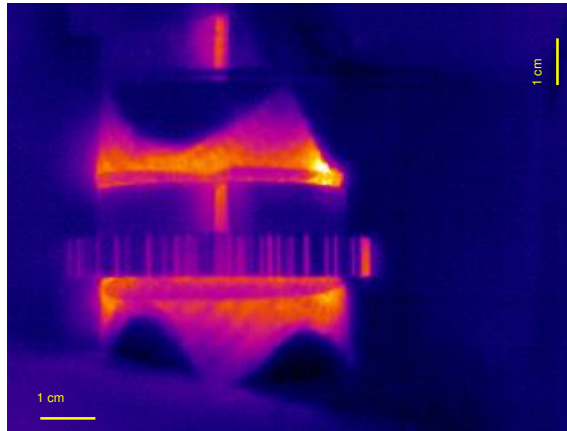
(b)
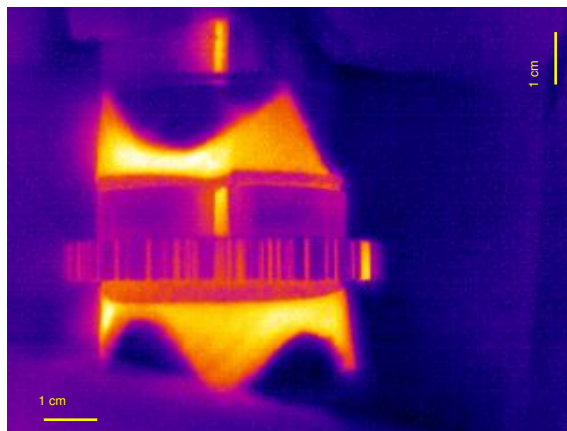
(c)

Figure 4.16: (a) IR recording from a complex gear at $t = 0\,sec.$, (b) at $t = 2\,sec.$, and (c) at $t = 10\,sec.$

The major limitations of an IR detection system are the line-of-sight requirement and the reflections in low emissivity materials. The first type of parts tested in this case are flawed along the surface of the gear teeth where the reflections are at a maximum. Also, the method chosen to inject the current into the part is not optimal; it generates higher temperature gradients in that specific region. For the second type, where the crack is located along the corner between two levels (a very common area where defects occur due to powder transfer between levels in the compaction stage) the line of sight and reflections are also a major limitations.

Figure 4.16 summarizes a test sequence where we observe the reflections from the surface of the part, specifically in the teeth area. When the current step is applied, the temperature on the surface of the sample increases causing higher incident radiation, and consequently, increased reflection from adjacent gear teeth.

The setup was modified to detect cracks located near the surface of the gear tooth. The modification first involves directing the current to the specific area (to cause higher temperature gradients). Second, the IR camera points directly towards the area of interest. Figures 4.17 to 4.20 illustrate the resulting sequence of thermal images as well as the subsequent temperature profiles along the centerline.

(a)   (b)
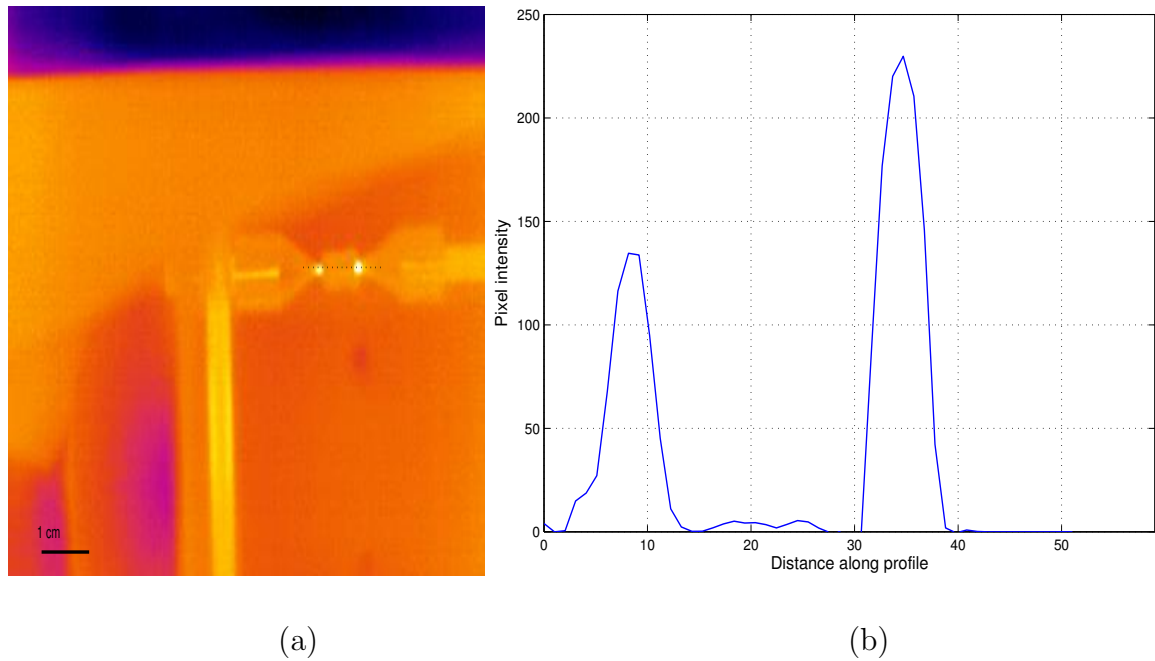
Figure 4.17: (a) IR recording at $t = 2\,sec.$, and (b) profile along the center line with a spatial pixel to pixel distance of $150\mu m$.

(a)   (b)
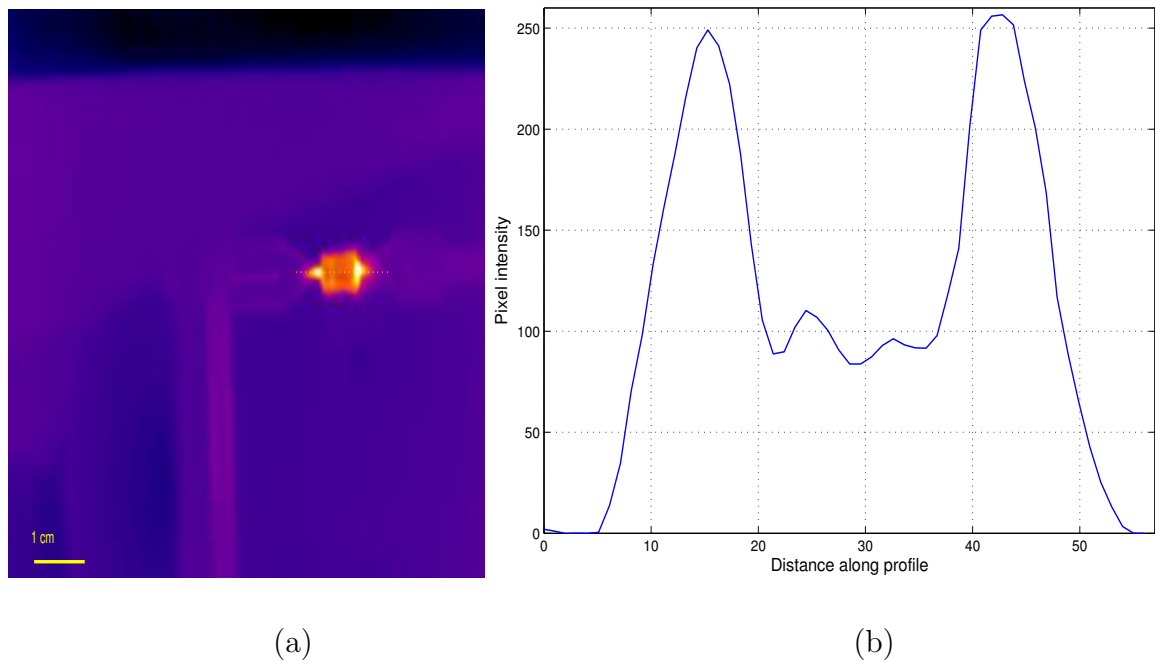
Figure 4.18: (a) IR recording at $t = 4\,sec.$, and (b) profile along the center line with a spatial pixel to pixel distance of $150\mu m$.

(a)   (b)
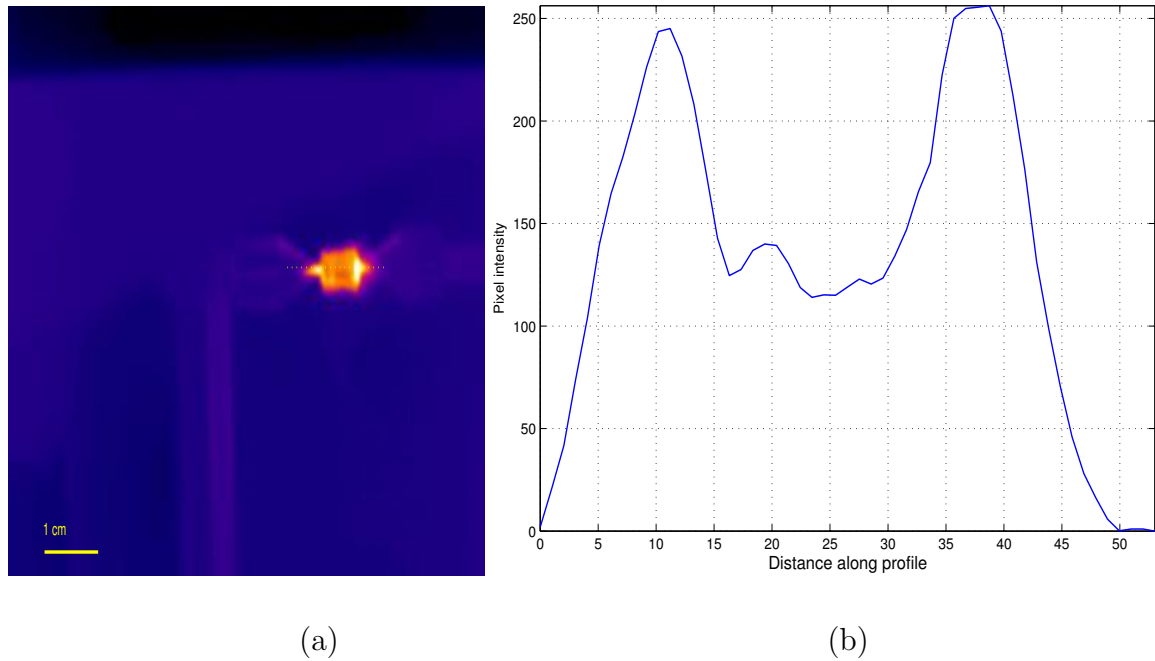
Figure 4.19: (a) IR recording at $t = 6\,sec.$, and (b) profile along the center line with a spatial pixel to pixel distance of $150\mu m$.

(a)   (b)

Figure 4.20: (a) IR recording at $t = 8\,sec.$, and (b) profile along the center line with a spatial pixel to pixel distance of $150\mu m$.

Chapter 5

Conclusions

The objective of this thesis is to establish the feasibility of using electric heating in P/M samples for the purpose of nondestructive material evaluation. In particular, this thesis developed an analytical formulation and numerical solutions for an IR imaging system as applied to the detection of defects in P/M compacts. The basic premise 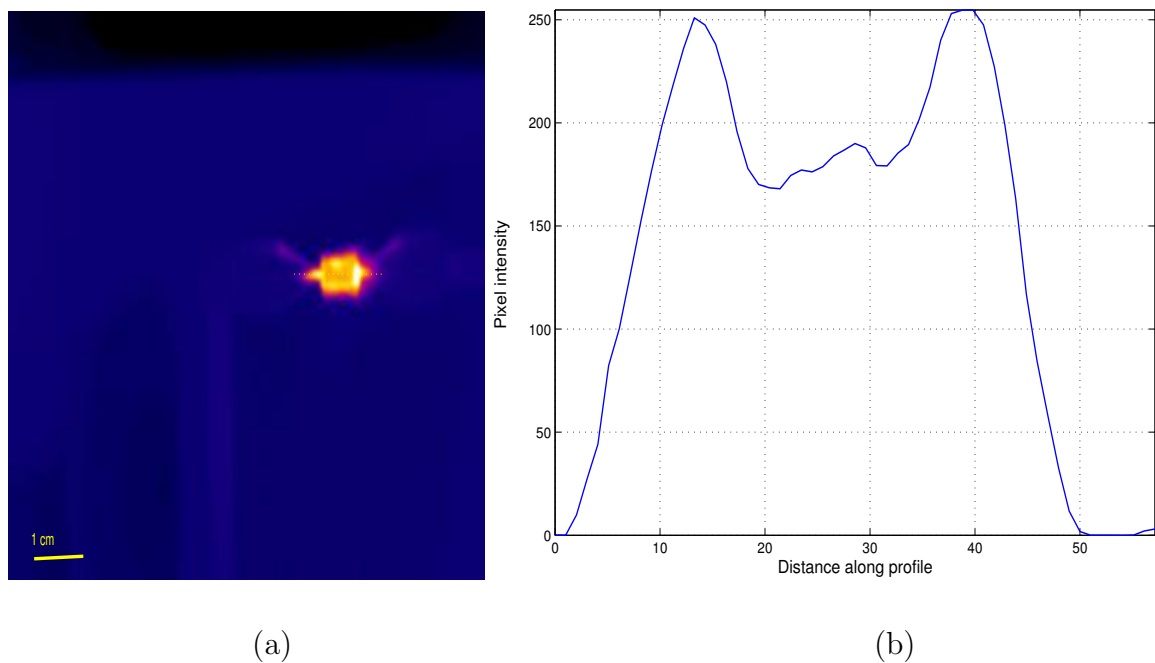was to inject DC current through the compact and to establish a thermal energy/ sample interaction. An IR camera can then capture the material response and display it as a thermal image over the surface of the part.

Specifically a mathematical finite element model was developed where the voltage and temperature distribution can be predicted throughout the volume of the P/M parts subject to a current input. This model is based on a DC current injection prescribed over a finite aperture of the part geometry. The numerical model was tested against an analytical solution of a cylinder. Next, the numerical model was extended to include an analysis related to the detection of thermal radiation emanating from the target as well as the surroundings, while taking into account the reflection caused by the part.

We successfully modeled the heat generation as a coupling between an electrostatic model and a heat transfer model. The numerical model presented in this work is

flexible in a sense that it can handle arbitrary current injection conditions and specification of material properties even on elemental level. The material data can be adjusted to fit both sintered and green-state compacts. Furthermore, the numerical modeling allows us to evaluate both steady-state and transient conditions.

The numerical model provided a theoretical test bed for the measurement system, specifically the infrared radiation. With the modeling results we are able to examine the sensitivity of the test; specifically we can explore detection limits in a steady state test arrangement. Moreover, the transient model enables us to establish the dynamic camera requirements.

The IR camera together with a power supply and data analysis software constituted the basic test arrangement. Through this setup we are able to conduct a number of critical experiments. For instance, steady state test revealed that surface cracks on the order of 20 microns can easily be detected. With additional signal processing steps it appears feasible that a fully automated evaluation system is possible. Although we have not yet tested compacts with subsurface cracks, the dynamic test with a pulsed current excitation should enable us to extend the sensitivity of the detection system to defects below the surface and increase its response time.

However, the test also revealed that the current injection method suffers the drawback of high contact resistance. This effect in conjunction with the non-uniformity of the sample density cause higher thermal gradients near the contact surfaces. As a result heating caused by small defects near the electric contacts is overshadowed. A second drawback is related to the emissivity of the sample which becomes a significant factor when evaluating complex parts such as gears (where reflections between the individual tooth elements can trigger false alarms).

In summary, it can be stated that the proof-of-concept IR testing system was successfully demonstrated. However, a fully manufacturing compliant and efficient system

will require further custom tailoring to meet the manufacturer's test environment.

This presented method is versatile; it can can be integrated into the fabrication process with no time penalty or cumbersome equipment.

It is important to observe that the use of this new testing testing technique has created another potential benefit: it can detect density variations in green-state parts. Controlling a uniform density is an active area of interest for many part manufacturers. We see the opportunity to map the thermal response into a density profile.

Further Work

One area of improvement is related to reducing the reflectivity of the part either through a special coating or by controlling the background. It also appears necessary to calibrate the method and reject radiation from the background as well as individual part elements. This can be accomplished by using a baseline picture obtained from a known good part; this image is then subtracted from the image obtained from the sample under test. The resulting difference can then be thresholded to minimize process variation.

Another area of improvement is the modification of the current injection scheme. Specifically it is desirable to minimize effects from the high contact resistance. A differential type of measurement, however, may already minimize theses effects. This can be theoretically investigated by modifying the existing numerical model through the inclusion of electrical contacts and material density variations. Furthermore, thermal radiance computations could be built into the model in order to take into account the IR camera system.

Bibliography

[1] Leuenberger, G. Ludwig, R. "Electrostatic Density Measurement in Green-State P/M parts" Final Report, Morris Boorky Powder Metallurgy Research Center, Consortium Meeting, April 9-10,2003, Metal Processing Institute, Worcester Polytechnic Institute.

[2] Leuenberger, G. "Electrostatic Density Measurement in Green-State P/M Parts" PhD thesis, ECE Department, Worcester Polytechnic Institute 2003.

[3] Leuenberger, G., Ludwig, R., Apelian, D. "Electrostatic Detection of Density Variations in Green-State Powder Metallurgy Compacts" Proceedings of QNDE 2001.

[4] Bogdanov, G. "Theoretical Basis and practical implementation of Electrical Impedance Material Inspection of powder Metallurgy Compacts" Master Thesis, ECE Department, Worcester Polytechnic Institute, 2000.

[5] Fei, M. "Electromagnetic Inspection, Infrared Visualization and Image Processing Techniques for Non Metallic inclusions in Molten Aluminum" Master Thesis, ECE Department, Worcester Polytechnic Institute 2002.

[6] Maldag, X.P.V. "Theory and Practice of Infrared Technology for Nondestructive Testing" John Wiley & Sons Inc. 2001.

[7] Burnay, S. G., Williams, T. L., Jones C. H. "Applications of Thermal Imaging " 10.P Publishing 1988.

[8] Carslaw, H., Jaeger, J. "Conduction of Heat in Solids" Second Edition, Oxford University Press 1959.

[9] Keith, F., Bohn, M.S. "Principals of Heat Transfer" Fifth Edition, PWS Publishing Company 1997.

[10] Arpaci, V.S. "Conduction Heat Transfer" Addison-Wesley Publishing Company 1966.

[11] Incropera, F.P., DeWitt, D.P. "Fundamentals of Heat and Mass Transfer" 4th edition, John Wiley & Sons, New York 1996.

[12] Sommerfeld, A. "Partial Differential Equations in Physics" Academic Press Inc. 1949.

[13] Logan, D A "First Course in Finite Elements Method" PWS Publishing Company 1993.

[14] German, R.M. "Powder Metallurgy Science" Metal Powder Industries Federation, Princeton, New Jersey, 1984.

[15] Clark, F. "Advanced Techniques in Powder Metallurgy" Rowmann and Littlefield Inc. New York, NY 1963.

[16] Myers, G.,E. "Analytical Methods in Conduction Heat Transfer"Genium publishing Corp. 1987.

[17] Gochenbach, M., S. "Partial Differential Equations: Analytical and Numerical Methods" Society for Industrial and Applied Mathematics, 2002.

[18] Siegel, R. and Howell, J. "Thermal Radiation Heat Transfer" Fourth Edition, Taylor & Francis 2002.

[19] Kraus, J.,D. "Electromagnetics" McGraw-Hill Book Company, Inc. 1953.

[20] Zahn, M. "Electromagnetic Field Theory: A problem solving approach" John Wiley & Sons, Inc. 1979.

[21] Bruhat,G. "Cours De Physique General: ELECTRICITE" Septieme Edition, Masson & C$^{\text{ie}}$. 1959.

[22] Chen, C.H. "Signal Processing and pattern Recognition in Non-destructive Evaluation of Materials" NATO ASI Series, Series F: Computer and Systems Sciences, Vol. 44. Springer-Verlag Berlin Heidelberg 1988.

[23] Siegel, R. and Howell, J. " Thermal Radiation Heat Transfer" 4th edition, Taylor & Francis. 2002.

[24] " FEMLAB User's Guide and Introduction" COMSOL Inc. version 2.2. 2001.

[25] Sullivan, J. Jr "Computational Methods For PDEs in Science and Engineering" ME 515 Course Notes. Worcester Polytechnic Institute, Fall 2003.

[26] "Cost-efficient, Net-shape Manufacturing with Powder Metals...a Primer" GKN Sinter Metals P/M University 2003.

[27] Lee Dong-Ho "Thermal Analysis of Integrated-Circuit Chips Using Thermographic Imaging Techniques", IEEE Transactions on Instrumentation and Measurement, Vol. 43, No. 6, December 1994.

[28] Gailius, A. and Zukauskas, D. "Determination of Concrete Structural Defects By Infrared Spectrum Analysis" ISSN 1392-1320 Materials Science (Medziagotyra). Vol. 9, No. 1. 2003.

[29] Ringermacher, H.I., Howard, D.R. and Gilmore, R.S., "Discriminating Porosity in Composites Using Thermal Depth Imaging" CP 615, Review of Quantitative Nondestructive Evaluation, Vol. 21, ed. by Thompson and D.E Chimenti. American Institute of Physics. 2002.

[30] Han, X., Favro L.D., and Thomas, R.L., "Recent Developments in Thermosonic Crack Detection" CP 615, Review of Quantitative Nondestructive Evaluation, Vol. 21, ed. by Thompson and D.E Chimenti. American Institute of Physics. 2002.

[31] Sun, I.G "Analysis of Quantitative Measurements of Defects by Pulsed Thermography Imaging" CP 615, Review of Quantitative Nondestructive Evaluation, Vol. 21, ed. by Thompson and D.E Chimenti. American Institute of Physics. 2002.

[32] Scott, R.J., "Nichols Portland: Parker Hannifin Corp." 2400 Congress Street, Portland, ME 04102.

[33] Traxler, H. "PLANSEE Aktiengesellschaft" A-6600 Reutte/ Tirol, Austria.